

CHANDRA X-RAY SOURCES IN THE COLLAPSED-CORE GLOBULAR CLUSTER M30 (NGC 7099)

PHYLLIS M. LUGGER AND HALDAN N. COHN

Indiana University, Department of Astronomy, 727 E. Third St., Bloomington, IN 47405; lugger@astro.indiana.edu

CRAIG O. HEINKE

Northwestern University, Department of Physics & Astronomy, 2145 Sheridan Rd., Evanston, IL 60208

AND

JONATHAN E. GRINDLAY AND PETER D. EDMONDS

Harvard-Smithsonian Center for Astrophysics, 60 Garden St., Cambridge, MA 02138

Draft version September 4, 2018

ABSTRACT

We report the detection of six discrete, low-luminosity ($L_X < 10^{33}$ erg s⁻¹) X-ray sources, located within 12'' of the center of the collapsed-core globular cluster M30 (NGC 7099), and a total of 13 sources within the half-mass radius, from a 50 ksec *Chandra* ACIS-S exposure. Three sources lie within the very small upper limit of 1.''9 on the core radius. The brightest of the three core sources has a luminosity of L_X (0.5–6 keV) $\approx 6 \times 10^{32}$ erg s⁻¹ and a blackbody-like soft X-ray spectrum, which are both consistent with it being a quiescent low-mass X-ray binary (qLMXB). We have identified optical counterparts to four of the six central sources and a number of the outlying sources, using deep *Hubble Space Telescope* and ground-based imaging. While the two proposed counterparts that lie within the core may represent chance superpositions, the two identified central sources that lie outside of the core have X-ray and optical properties consistent with being CVs. Two additional sources outside of the core have possible active binary counterparts. We discuss the X-ray source population of M30 in light of its collapsed-core status.

Subject headings: globular clusters: individual (M30, NGC 7099) — X-rays: binaries — novae, cataclysmic variables — stars: neutron

1. INTRODUCTION

M30 (NGC 7099) is one of 21 Galactic globular clusters that show strong evidence of having undergone core collapse (Djorgovski & King 1986; Lugger et al. 1995). The collapsed state of the core has been confirmed by *Hubble Space Telescope* (*HST*) imaging (Yanny et al. 1994; Sosin 1997; Guhathakurta et al. 1998). Sosin (1997) has placed an upper limit of 1.''9 (0.08 pc) on the core radius of M30 from high-resolution *HST* Faint Object Camera imaging. The extraordinarily high central density of M30, which may exceed $\sim 10^6 M_\odot \text{pc}^{-3}$, makes its core and the surrounding power-law cusp one of the highest density environments in the Galaxy. A high rate of stellar interactions is expected in the core and cusp regions, resulting in blue straggler formation via stellar mergers, binary formation via tidal capture and/or 3-body interactions, and binary interactions such as exchange encounters (Hut et al. 1992). M30 shows some of the strongest evidence of stellar interactions seen in any globular cluster. It has a very high blue straggler frequency, a very large bluer-inward color gradient, and a large deficit of bright giants in the inner region (Guhathakurta et al. 1998; Howell et al. 2000). Thus, the central region of M30 is expected to be a conducive environment for the formation of X-ray binaries.

Like the nearby collapsed collapsed-core globular cluster NGC 6397, M30 does not contain any bright ($L_X \gtrsim 10^{35}$ erg s⁻¹) low-mass X-ray binaries (LMXBs). This opens the possibility of studying the distribution of low-luminosity sources near the center of M30, which would be hindered by the presence of bright sources. Previous ROSAT observations of M30 detected low-luminosity X-ray emission from the vicinity of the core, with about 10'' positional accuracy (Johnston et al. 1994; Verbunt 2001). Since this is compara-

ble to the size of the cusp region, the ROSAT detection is consistent with either a single source or a centrally concentrated source population. In order to further investigate the X-ray source population of M30, we have obtained and analyzed a medium-depth *Chandra*-ACIS exposure. As expected, we detected a central population of X-ray sources. We describe the X-ray data, analysis method, and results in the following sections.

2. DATA

We obtained a 49.4 ksec ACIS-S¹ exposure of M30 on 2001 Nov 11, with the center of the cluster placed in the S3 chip. We chose the back-illuminated S3 chip for its high sensitivity and spectral resolution. The cluster center was offset by -0.''7 in the Y-coordinate from the nominal ACIS-S aimpoint, to ensure that the half-mass region of the cluster was well covered by the chip. The location of the cluster center was approximately 2.''5 from the nearest chip edge. We used the timed exposure mode with the faint telemetry format. The low reddening ($E(B-V) = 0.03$) toward M30 results in a low neutral hydrogen column density, $N_H \approx 1.7 \times 10^{20}$ cm⁻². We have adopted a distance 9.0 ± 0.5 kpc for M30, based on the *Hipparcos* results of Carretta et al. (2000). Our adopted detection threshold of 4.5 counts, for the 49.4 ksec ACIS-S exposure, translates to a flux of $F_X \approx 4 \times 10^{-16}$ erg s⁻¹ cm⁻² in the 0.5–6 keV energy band, for a range of spectral models, e.g. a 6 keV thermal plasma spectrum. This limiting flux corresponds to a luminosity of $L_X \approx 4 \times 10^{30}$ erg s⁻¹.

¹ Advanced CCD Imaging Spectrometer/S-Array

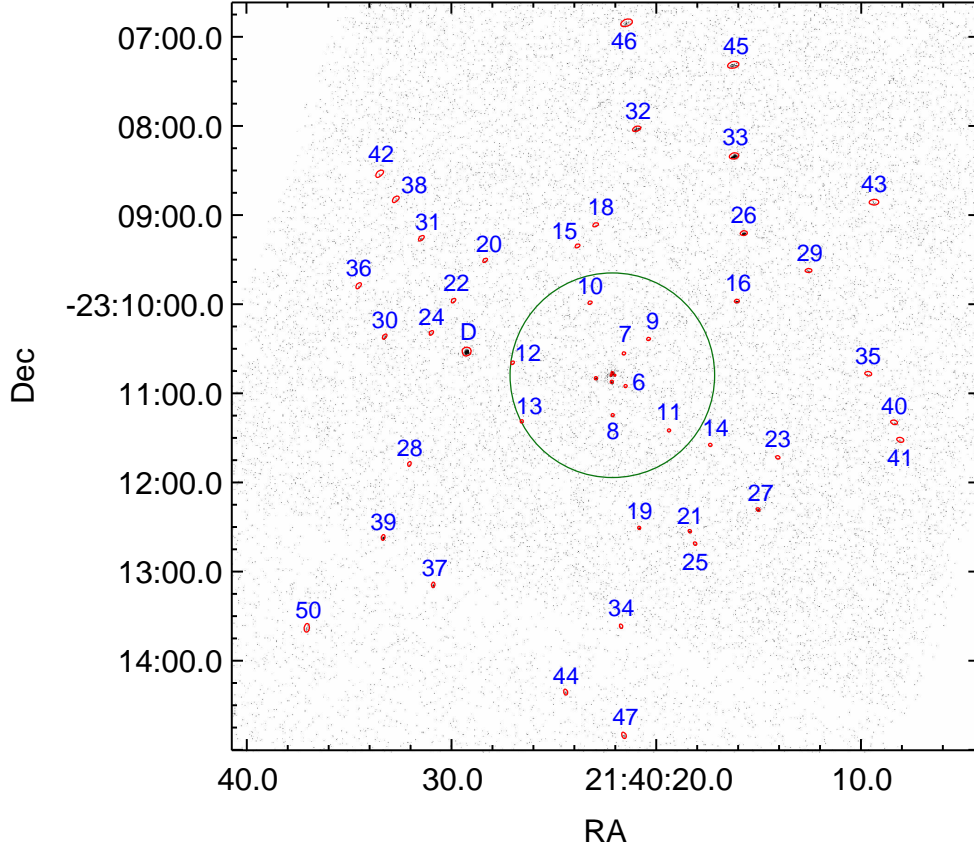


FIG. 1.— *Chandra* ACIS-S image of M30 and the surrounding region in the 0.3–7 keV energy band. The cluster half-mass radius of $1'.15$ is indicated by the circle. The extraction regions for the detected sources are indicated by small polygons and are labeled by the source numbers from Table 1. The five central sources are labeled in Fig. 2. Source D is the brightest object in the field. (See the electronic edition of the *Journal* for a color version of this figure.)

3. *Chandra* DATA ANALYSIS AND RESULTS

3.1. Basic Processing

We reprocessed the data from level 1 data products using the CIAO 3.2 software², using current calibration files and excluding the pixel randomization that is performed in the standard processing to remove the artificial substructure introduced by the precession of the spacecraft. An exposure of 50 ksec includes a sufficient number of dither cycles (~ 50) to smooth out the substructure without additional randomization. The exclusion of randomization is expected to sharpen the image slightly, which is useful in this case because of potential source image crowding in the collapsed core region. We used the `acis_run_hotpix` CIAO script to identify bad columns and bad pixels, and removed these as well as events not exhibiting one of the standard ASCA grades. We also applied time-dependent gain corrections and charge transfer inefficiency corrections where appropriate. Periods of high background were searched for, but none was found.

The *Chandra*-ACIS X-ray background is energy dependent, with a fairly sharp rise above 7 keV. Figure 1 shows an $8'.5 \times 8'.5$ region about the cluster center, in the 0.3–7 keV energy band, with the cluster half-mass radius ($r_h = 1'.15$; Harris 1996) indicated and the detected sources labeled with the numbers from Table 1. There is a strong concentration of sources about the cluster center, with a decreasing density toward the half-mass radius. Figure 2 shows a central

$32'' \times 32''$ region of the ACIS-S image with the standard $0''.5$ binning. Three bright central sources (labeled A1, B, and C) are clearly visible and two additional fainter sources (A2 and A3) are seen within the core. We shall refer to the brightest source in the field as source D.

The optical center of the cluster is located about $1''.8$ (3.6 pix) south of the centroid of the brightest source A1, as determined from our boresight correction (see §4.1). Figure 3 shows a comparison of images of the central region in low- and high-energy bands (0.3–2.5 keV versus 2.5–7 keV). Note that source A1 nearly disappears in the high-energy band, indicating that it has an extremely soft spectrum. As discussed below, this provides strong evidence that it is a quiescent low-mass X-ray binary (qLMXB).

3.2. Source Detection

We used the CIAO WAVEDETECT (Freeman et al. 2002) and PWDETECT (Damiani et al. 1997) utilities for detecting sources in the 0.3–7 keV band, after experimenting with several choices of detection bands and source detection programs. We used spatial scales of 1, 1.4, 2, and 2.8 pixels for both the WAVEDETECT and PWDETECT runs. We find that PWDETECT is very effective at identifying faint X-ray sources within a few arcseconds of brighter sources, but appears to identify some spurious sources and to miss real sources when applied across large fields. WAVEDETECT appears to have a more accurate algorithm for detecting faint uncrowded X-ray sources without false detections. The source A2 (but not A3) is detected in the 2.5–7 keV energy band (but

² <http://cxc.harvard.edu/ciao/>

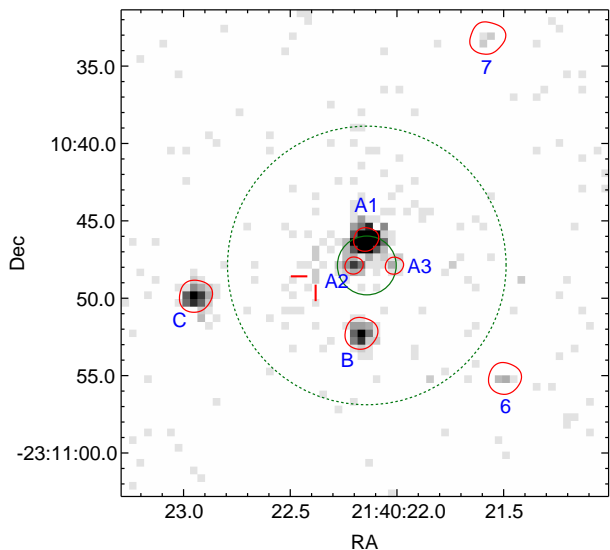


FIG. 2.— The central $32'' \times 32''$ region of the *Chandra* ACIS-S image of M30 in the energy band 0.3–7 keV. The cluster core radius upper limit of $1''.9$ is indicated by the central circle. The extraction regions for the detected sources are indicated by polygons. The possible millisecond pulsar X-ray counterpart that has been reported by Ransom et al. (2004) is indicated by the tick marks to the left of source A2. The dashed circle has a radius of $9'' = 5 r_c$ and is used in the estimation of possible unresolved flux (§3.7). (See the electronic edition of the *Journal* for a color version of this figure.)

not in softer or broad-band images) by WAVDETECT, while PWDETECT detects both A2 and A3 in broad-band images.

We ran PWDETECT on the S3 chip, and WAVDETECT on a circular region with radius $4''.5$ centered on the cluster (i.e. extending out to $3.9 r_h$). We also ran WAVDETECT on an image of the entire ACIS-S detection array (6 chips), binned by a factor of two to accommodate the increasing size of the *Chandra* point-spread function. The reason for extending beyond the S3 chip, in both WAVDETECT runs, was to search for possible *Chandra* source counterparts in the cluster halo. For each run, we choose a significance threshold designed to produce at most two false detections per image.

Our final source list includes the detections from the 0.3–7 keV WAVDETECT run, removing three sources that we judge spurious (one having less than four counts and two from spurious double detections of off-axis sources), and adding the sources A2 and A3 identified in the PWDETECT run. Fifty sources were detected within $4''.5$ of the cluster center, and these sources are listed in Table 1. An additional 46 sources were found on the remainder of the array, after rejecting spurious sources; these sources will be discussed elsewhere.

3.3. Source Properties

Table 1 (located at end of text) lists parameters for the 50 sources within $4''.5$ of the cluster center, including position, distance from the cluster center (see §4.1), counts in the 0.3–7 keV band, X-ray flux, X-ray color indices, and other identifiers. Of these sources, 13 lie within the cluster half-mass radius and are thus the most likely candidates to be actual cluster members.

Source extractions were performed using the IDL script ACIS_EXTRACT³ (Broos et al. 2002), which uses CIAO and

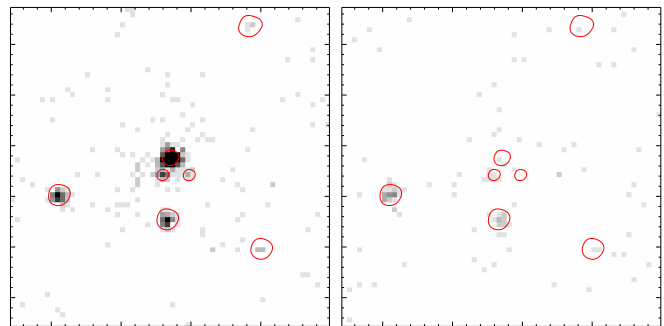


FIG. 3.— A comparison of *Chandra* images of the central $32'' \times 32''$ region of M30 in low-energy versus high-energy bands. The left panel shows the 0.3–2.5 keV band and the right panel shows the 2.5–7 keV band. The source extraction regions are as in Fig. 2. Note that the likely qLMXB, source A1 in Fig. 2, nearly disappears in the high-energy band. (See the electronic edition of the *Journal* for a color version of this figure.)

FTOOLS⁴ tools and TARA⁵ IDL software. We follow the general procedures of Feigelson et al. (2002); we briefly discuss the method here. Point-spread functions (psfs) were generated for each source, and polygonal extraction regions were generated to match the 90% encircled-energy contour (at 1.5 keV) for most sources. For a few bright sources, we chose a larger encircled energy; for sources A1, A2, and A3 we chose a smaller region due to crowding.

We refined the positions of all sources by iteratively centroiding the counts within the extraction regions. Event lists, spectra, and light curves were extracted for each source, and response files, background spectra, and effective area files were constructed for each source using current (CALDB 3.03) quantum efficiency degradation corrections and the new MKACISRMF tool to generate responses. The psf fraction enclosed by the extraction regions was calculated at five energies and interpolated for other energies, and the effective area functions were altered to take account of these aperture corrections.

We computed background-subtracted photometry for each source in several bands. X-ray energy fluxes for each source were derived by computing photon fluxes in seven relatively narrow bands. We computed the transformation from photon fluxes to unabsorbed energy fluxes for each band, assuming the photoelectric absorption appropriate for the distance to M30, for two very different spectra: a 6 keV thermal plasma spectrum and a 10^6 K hydrogen-atmosphere spectrum. The differences between the transformation coefficients were less than 4% for bands below 2 keV, and less than 7% for higher energy bands. We adopted the 6 keV thermal plasma spectrum and summed the unabsorbed energy fluxes (and errors) from each band to obtain the fluxes (and errors) presented in Table 1.

Relatively few sources in our field exhibit clear signs of variability. A Kolmogorov-Smirnov test (from ACIS_EXTRACT), which was applied to the light curve of each source, finds that only 3 of 50 sources show variability at the 99% confidence level or higher, viz. sources 37, 39, and 40 (CXOU J214030.86-231308.2, 214033.30-231236.3, and 214008.37-231118.9, respectively); all three are located beyond $3'$ from the cluster center. Of these, source 39 has a likely identification as a bright foreground star (see §§3.6.2, 4.7).

³ Version 3.65, http://www.astro.psu.edu/xray/docs/TARA/ae_users_guide.html

⁴ Version 5.2, http://heasarc.gsfc.nasa.gov/docs/software/ftools/ftools_menu.html

⁵ <http://www.astro.psu.edu/xray/docs/TARA/>

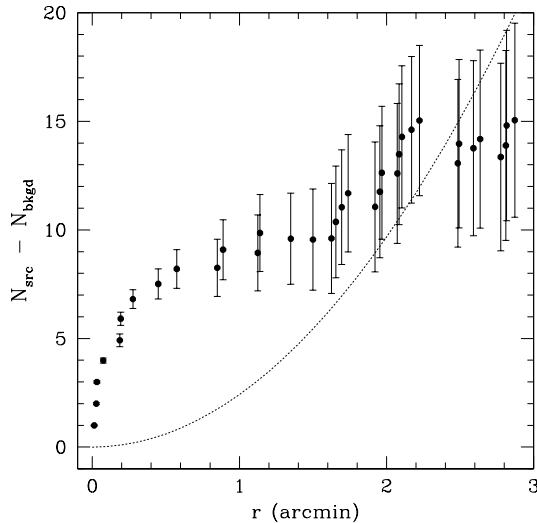


FIG. 4.— Cumulative radial distribution of excess *Chandra* source counts over the background predicted from the Giacconi et al. (2001) extragalactic source counts. Error bars represent the statistical uncertainty of the background correction. The dashed curve is the cumulative background distribution for the expected background density of 0.77 arcmin^{-2} .

In order to estimate the number of sources that are likely members of M30, we computed the expected background density of extragalactic sources based on Giacconi et al. (2001). Their counts predict a background source density of $N_{\text{bkgd}} = 0.77 \text{ arcmin}^{-2}$ detected above 4.5 counts in the 0.3–7 keV band, corresponding to a flux limit $4.0 \times 10^{-16} \text{ erg s}^{-1} \text{ cm}^{-2}$ in the 0.5–6 keV band for a power-law spectrum with photon index 1.7. Fig. 4 shows the cumulative radial distribution of the excess number of sources over the background level. The cumulative excess source profile flattens at about $1'$, in agreement with the expectation that the source distribution should be concentrated within the half-mass radius ($r_h = 1'15$). Fig. 4 indicates that the background-corrected number of cluster sources within r_h is about 10 ± 2 , where the expected number of background sources within r_h is 3.2. (We note that the error represents the statistical uncertainty in the background correction only.) For comparison, Pooley et al. (2003) report the detection of a total of 7 sources within the half-mass radius of M30 to a limiting luminosity of $4 \times 10^{30} \text{ erg s}^{-1}$ (0.5–6 keV; which corresponds to a flux limit of $4 \times 10^{-16} \text{ erg s}^{-1} \text{ cm}^{-2}$ for our adopted cluster distance of 9.0 kpc), based on an analysis of the same *Chandra* observations reported here. They estimate that 1–2 of these are background objects, using extragalactic source counts from Giacconi et al. (2001). We note that two of our detected sources are located just inside of r_h , as seen in Fig. 1, and thus may not have been counted by Pooley et al. (2003).

It can be seen from Fig. 4 that there is a second rise in the excess number of sources over the expected background between r_h and $2r_h$. While the Giacconi et al. (2001) counts predict a total of 9.6 extragalactic sources in this region, the actual number of detected sources is 14. This excess persists if we adopt a higher flux limit of $10^{-15} \text{ erg s}^{-1} \text{ cm}^{-2}$ (0.5–6 keV), for which 4.5 sources are predicted while 9 are detected. While this difference does not have a high level of statistical significance, we note that similar overdensities of sources interpreted as belonging to the background population have been seen outside the half-mass radii of other globular clusters (Gendre et al. 2003; Heinke et al. 2003a, 2005),

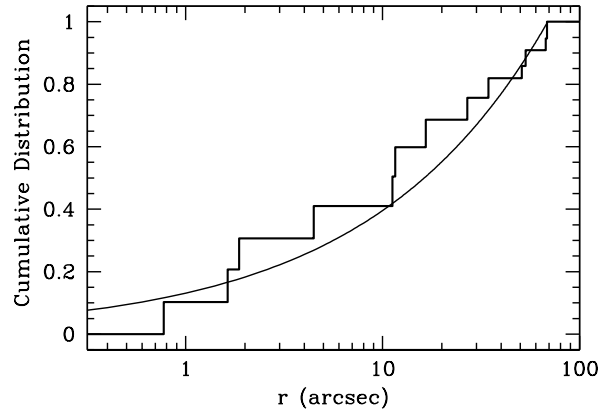


FIG. 5.— Cumulative, background-corrected radial distribution of *Chandra* sources in M30 (stairstep) with a power-law fit (smooth curve). The maximum-likelihood, power-law slope is -1.52 ± 0.14 , from which we infer a mean source mass of $1.27 \pm 0.16 M_{\odot}$ (see text).

suggesting that some of these objects may actually be X-ray sources in the cluster halo. Such sources might have been ejected into the halo from the central regions or else might naturally reside in the halo owing to their low masses. Brandt & Hasinger (2005) have reviewed the issue of possible cosmic variance in the extragalactic source counts, concluding that there is some evidence for significant number fluctuations below fluxes of about $10^{-15} \text{ erg s}^{-1} \text{ cm}^{-2}$. In light of this, we also investigated by how much the background source density would have to be increased to eliminate the apparent excess of sources beyond r_h . This would require that the density be increased by about 30% (which is within the variance range discussed by Brandt & Hasinger 2005), which would increase the expected background number within r_h to 4.2. Such an upward adjustment in the background count level would reduce the likely source population within r_h by just one source.

3.4. Source Spatial Distribution

As in our previous studies of globular cluster X-ray source distributions, we have analyzed the radial distribution of the likely cluster sources by fitting models to the two-dimensional source distribution using maximum-likelihood techniques (c.f. Grindlay et al. 2002). Given the small sample size (~ 10 sources above background within r_h) and the small optical core radius of M30 ($\lesssim 2''$), we have fit a pure power-law model. We took the background level to be that given by the Giacconi et al. (2001) extragalactic source counts, as discussed in §3.3, and use the Monte-Carlo procedure described in Grindlay et al. (2002) to correct for background. The best-fit power-law slope of the source surface density profile $S(r)$ is $\alpha = d \ln S / d \ln r = -1.52 \pm 0.14$; the uncertainty represents the 68% range about the median value for 1000 bootstrap resamplings of the source sample. Figure 5 shows this fit to the cumulative source distribution, demonstrating that it provides a good fit to the profile. Since M30 is a collapsed-core cluster, the relation between cusp slope and object mass presented by Cohn (1985) is appropriate; we have previously applied this analysis to the source distribution in the collapsed-core cluster NGC 6397 (Taylor et al. 2005). The predicted slope of a

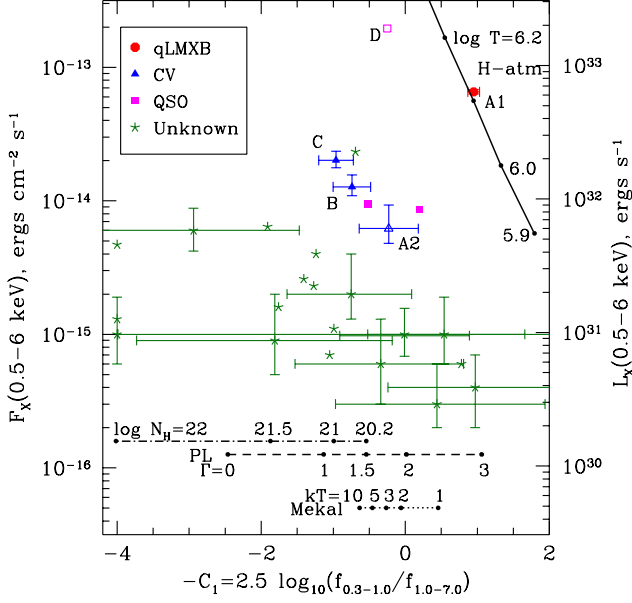


FIG. 6.— X-ray color-magnitude diagram for sources within 2 half-mass radii ($2/3$) of the center of M30. The abscissa is the negative of the index C_1 defined by Eqn. 2, the left-hand ordinate is the 0.5–6 keV flux, and the right-hand axis gives the X-ray luminosity for an assumed distance of 9.0 kpc. Sources with no soft counts are plotted with an X-ray color of $-C_1 = -4$. Filled symbols are used for sources with a likely identification and open symbols for sources with a plausible identification. Errors are plotted for sources lying within the $1/15$ half-mass radius of M30. Other lines indicate the colors of MEKAL thermal plasma spectra, power-law spectra, and intrinsically absorbed power-law spectra, or the color and luminosity of a 10 km NS with a hydrogen atmosphere in M30. (See the electronic edition of the Journal for a color version of this figure.)

component with mass m is,

$$\alpha = -1.89 \frac{m}{m_d} + 0.65, \quad (1)$$

where m_d is the mass of the component that dominates the cusp potential, for which $\alpha = -1.23$. Sosin (1997) has determined a cusp slope of -0.70 ± 0.08 for a turnoff mass group in M30. From this value and an assumed turnoff mass of $0.79 \pm 0.05 M_\odot$ from Bergbusch & Vandenberg (1992, assuming a cluster age of 14 Gyr), we may infer from Eqn. 1 that the cusp is dominated by stars with characteristic mass $m_d = 1.11 \pm 0.10 M_\odot$; we interpret this as representing an admixture of massive white dwarfs and neutron stars. Our measured slope of -1.52 ± 0.14 for the X-ray sources then implies a characteristic source mass of $m_x = 1.27 \pm 0.16 M_\odot$. Given the range of uncertainty, this includes both CVs and LMXBs.

We note that the surface-brightness profile of M30 steepens significantly from the central cusp slope beyond ~ 0.5 from the cluster center (Lugger et al. 1995). Thus, the measured slope for the source population within the $1/15$ half-mass radius may be best interpreted as the mean slope for the cusp and the immediately surrounding region. Overall, the measured cusp slope suggests that the characteristic X-ray source mass is either comparable to or somewhat higher than that of the typical object that dominates the cusp.

3.5. X-ray Color Indices

In order to provide some quantification of the X-ray source spectral properties, we computed X-ray color indices following the approach of other studies (e.g. Grindlay et al. 2001a, 2002). Since the majority of detected sources are expected

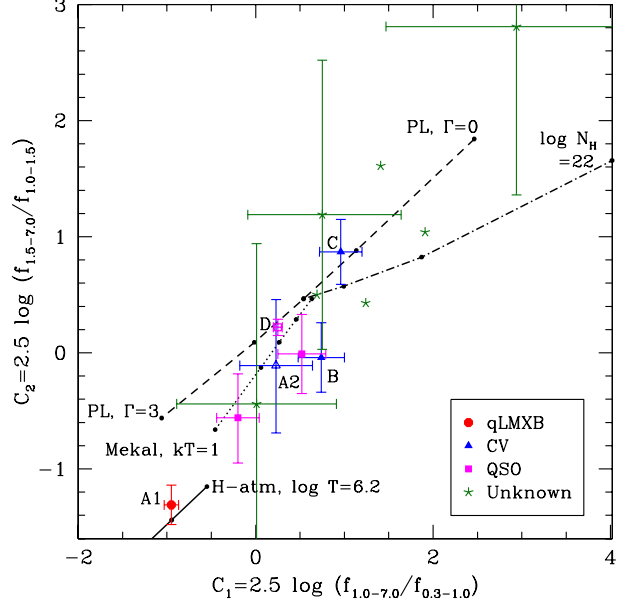


FIG. 7.— X-ray color-color diagram for sources with at least 10 total counts located within 2 half-mass radii ($2/3$) of the center of M30. The abscissa and ordinate are the indices C_1 and C_2 defined by Eqn. 2. Filled symbols are used for sources with a likely identification and open symbols for sources with a plausible identification. Errors are plotted for sources within the half-mass radius ($1/15$), and for the three objects we believe or suspect to be quasars. The expected colors of various spectra are plotted, as in Fig. 6. (See the electronic edition of the Journal for a color version of this figure.)

to be nonmembers, at a large range of distance, a distance-independent color-color diagram provides a useful adjunct to a color-magnitude diagram. After some experimentation, we defined two indices by,

$$C_1 = 2.5 \log \left[\frac{f(1.0 \text{ keV} - 7.0 \text{ keV})}{f(0.3 \text{ keV} - 1.0 \text{ keV})} \right] \quad (2a)$$

$$C_2 = 2.5 \log \left[\frac{f(1.5 \text{ keV} - 7.0 \text{ keV})}{f(1.0 \text{ keV} - 1.5 \text{ keV})} \right]. \quad (2b)$$

The index C_1 is designed to be sensitive to low-energy absorption below 1 keV, while C_2 is designed to be sensitive to the spectral slope at higher energy. The particular bands were chosen to provide adequate signal-to-noise for both soft- and hard-spectrum sources. Figures 6 and 7 show the color-flux and color-color diagrams, respectively, for all sources within two half-mass radii ($2/3$) of the cluster center (only sources with > 10 counts are plotted in Fig. 7).

We have plotted, in Figures 6 and 7, the colors where various model spectra would be expected to fall, including a power law with photon index $\Gamma = 0, 1, 1.5, 2$, and 3 ; a thermal plasma spectrum (MEKAL code, Phillips et al. 1999), with the low metallicity of M30 (1.5% solar for α -elements) and temperatures of 1, 2, 3, 5, and 10 keV; and a hydrogen-atmosphere spectrum (NSATMOS, Rybicki et al. 2005) with temperatures of $\log T = 5.9, 6.0, 6.1$ and 6.2 . We have plotted both color and luminosity for hydrogen-atmosphere neutron star spectra in Figure 6, for an assumed $1.4 M_\odot$, 10 km radius neutron star at a distance of 9.0 kpc. We have also plotted the effects of increasing N_H upon a power-law model of photon index 1.5, typical of quasars or CVs that may suffer intrinsic absorption, from the cluster standard of $1.7 \times 10^{20} \text{ cm}^{-2}$ to $10^{21}, 3 \times 10^{21}$, and 10^{22} cm^{-2} .

As discussed in §3.6 and §4, we have identified a likely qLMXB (source A1) and two likely CVs (sources B and C). Source A1 (plotted as a filled circle) has the softest X-ray colors of any of the objects in Figs. 6 and 7 and lies on the expected track of a 10 km neutron star with a hydrogen atmosphere, consistent with a qLMXB interpretation (Heinke et al. 2003c). The high flux of this object allowed detailed spectral analysis, as described in §3.6.1. The two likely CVs, sources B and C, have similar color index values, which are considerably harder than that of source A1 and approximately consistent with a ~ 10 keV MEKAL spectrum or a power law of index 1.5. The general similarity of the colors of source A2 (plotted as an open triangle) to those of sources B and C (filled triangles), combined with its nearly certain cluster membership, suggests that it may also be a CV. We discuss its possible positional coincidence with a moderately bright, extremely blue star in §4.3 below.

The two sources that we believe are quasars, based on their optical spectra (see §4.7), are plotted as filled squares, while source D, which appears more likely to be a quasar than a CV based on its optical spectrum (see §4.6), is plotted as an open square. Source D and one of the two likely quasars are indistinguishable from CVs through their X-ray colors, while the other likely quasar has a softer spectrum, suggestive of a photon index between 2 and 3 or a very low-temperature MEKAL spectrum. This difference in X-ray color evidently indicates a difference in the intrinsic reddening and/or the X-ray emission mechanism in these three likely quasars. We note that the fainter X-ray sources lying beyond the half-mass radius (indicated by the star symbols without error bars in Fig. 6), which are probably predominantly active galactic nuclei, show relatively harder spectra, consistent with the results of *Chandra* extragalactic surveys (Giacconi et al. 2001; Kim et al. 2004).

The similarity of the colors of likely quasars with those of likely CVs indicates that color indices alone cannot be used to distinguish between these source classes. This ambiguity must be resolved by other means, including optical identification, photometry, and spectroscopy.

3.6. X-ray Spectral Analysis

We fit energy spectra for the brightest sources in XSPEC, binning the spectra to have 5, 10, 20 or more counts per bin and ignoring data above 8 keV. For each fit we fix the photoelectric absorption to be greater than or equal to the known N_H column density in the direction of M30, $1.7 \times 10^{20} \text{ cm}^{-2}$.

3.6.1. A1, a quiescent low-mass X-ray binary

The relatively bright source A1 (CXOGLB J214022.13-231045.5) has an X-ray color, luminosity, and spectrum similar to many quiescent low-mass X-ray binaries identified in other globular clusters such as NGC 6440 (in't Zand et al. 2001), ω Cen (Rutledge et al. 2002), and 47 Tuc (Heinke et al. 2003b) with typical $L_X = 10^{32-33} \text{ erg s}^{-1}$ (Heinke et al. 2003c). Its location within about $1''.8$ from the center of M30 identifies it as a certain cluster member.

The neutron stars (NSs) in qLMXBs are believed to be radiating heat stored in their core from prior accretion episodes (Brown et al. 1998), or perhaps to be accreting at extremely low levels (Campana et al. 1998). NSs accreting hydrogen-rich material will develop outer atmospheres of pure hydrogen (due to the rapid stratification of elements in the atmosphere, Romani 1987) which will determine the X-ray spectrum. Hydrogen atmospheres shift the peak of the blackbody-like spectrum emitted from the NS surface to higher frequen-

TABLE 2
M30 A1 HYDROGEN ATMOSPHERE
MODELS

Model Parameter	M fixed	R fixed
Rybicki NSATMOS model		
kT (eV)	94^{+17}_{-12}	124^{+18}_{-16}
$N_H^{a,b}$ (10^{20} cm^{-2})	$2.9^{+1.7}_{-1.2}$	$2.9^{+1.6}_{-1.2}$
R_{NS} (km)	$13.4^{+4.3}_{-3.6}$	(10.0)
M_{NS} (M_\odot)	(1.4)	$2.04^{+0.45}_{-0.72}$
χ^2_ν/dof	1.00/30	1.00/30
Null hyp. prob.	47%	46%
Blackbody model		
kT (eV)	191^{+8}_{-9}	
N_H^a (10^{20} cm^{-2})	$1.7^{+0.7}_{-0}$	
R_∞^b (km)	$2.4^{+0.3}_{-0.2}$	
χ^2_ν/dof	1.38/30	
Null hyp. prob.	7.8%	

NOTE. — All errors are 90% confidence limits. Distance of 9.0 kpc is assumed. In each column, either the mass or the true radius of the neutron star is held fixed.

^a N_H restricted to be greater than the galactic column density in the direction of M30, $1.7 \times 10^{20} \text{ cm}^{-2}$.

^b Reached hard limit of model.

cies, due to the strong frequency dependence of free-free absorption (Rajagopal & Romani 1996; Zavlin et al. 1996). Rutledge et al. (1999) have shown that the inferred radii from hydrogen-atmosphere spectral fitting of known qLMXBs in our galaxy are consistent with the canonical 10 km NS radius, while blackbody fits produce smaller inferred radii.

We have attempted to fit the spectrum of A1 (binned to have 20 counts per bin) with several single-component models, each including absorption and a (small, 2%) pileup correction (with the pileup grade migration parameter α fixed to 0.5; see Davis 2001). Source A1 cannot be adequately fit by an absorbed power law; the best such fit (with a photon index of 4.9) gives $\chi^2_\nu = 2.23$ for 30 degrees of freedom, and a null hypothesis probability of 10^{-4} . Bremsstrahlung or MEKAL models (using an abundance of $[M/H] = -1.82$ for the cluster, Harris 1996; Carney 1996) give acceptable χ^2_ν values (1.15), but rather low temperatures of 0.5 keV. Blackbody models give acceptable fits, but with rather small inferred radii ($2.4^{+0.3}_{-0.2}$ km), and prefer a value for N_H below the cluster value.

The most physically plausible model for source A1 is a neutron star heated by accretion and radiating a blackbody-like spectrum through a hydrogen atmosphere. We find an excellent fit ($\chi^2_\nu = 1.00$) for the NSATMOS (Rybicki et al. 2005) model (see Fig. 8), the parameters of which are given in Table 2. No additional harder component (often modeled as a power-law of photon index 1–2 for other qLMXBs) is required; if a power-law component with photon index 2 is included in the fit, its contribution makes up no more than

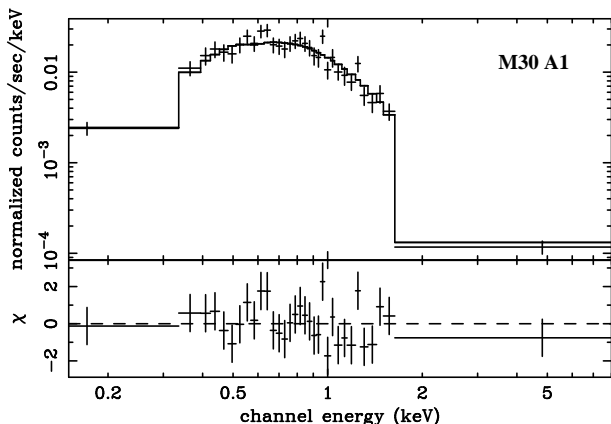


FIG. 8.— Spectral fit of a neutron star, hydrogen-atmosphere model (NSATMOS, Rybicki et al. 2005) for source A1 (upper panel); deviations from the fit (lower panel). The best-fit model parameters are given in Table 2.

20% the 0.5–10 keV unabsorbed flux (90% confidence).

The inferred unabsorbed 0.5–10 keV X-ray luminosity is $7.1 \times 10^{32} \text{ erg s}^{-1}$, and the inferred bolometric luminosity is $1.21 \times 10^{33} \text{ erg s}^{-1}$. If the mass is fixed at $1.4 M_{\odot}$ and distance is fixed at 9.0 kpc, the inferred radius is $13.4^{+4.3}_{-3.6} \text{ km}$, consistent with a canonical 10 km NS radius (but also with the higher range found for X7 in the cluster 47 Tuc, Rybicki et al. 2005). Alternatively, with the radius constrained at 10 km, a higher mass of $2.04^{+0.45}_{-0.72} M_{\odot}$ gives an acceptable fit. If neither mass nor radius is fixed in the fit, we obtain fairly broad 90% confidence ranges of $7.0 \text{ km} \leq R \leq 19.2 \text{ km}$ and $M \leq 2.8 M_{\odot}$.⁶ Fits with the NSA model (Zavlin et al. 1996) gave similar results for the range of parameter space consistent with the NSA model’s single adopted surface gravity (see Rybicki et al. 2005).

3.6.2. Other cluster sources

We fit the X-ray sources having more than 70 counts (including A1) with MEKAL and absorbed power-law spectra; the results are summarized in Table 3. Most were well-fit with MEKAL temperatures near 5 keV or power-law indices near 1.8, with N_H column densities roughly consistent with that expected toward M30. Two sources are rather softer, while one is harder.

The softest spectrum (besides the qLMXB) belongs to source 39 (CXOU J214033.30-231236.3), which we identify with a bright foreground star below (§4.7). This spectrum is poorly fit by a power-law (due to significant emission lines at 0.8–0.9 keV), giving a photon index of 2.6, and a reduced χ^2 of 2.6. Fitting with a MEKAL spectrum of solar abundance provides acceptable fits $\chi^2_{\nu} \sim 1.1$, for a kT of $0.7^{+0.13}_{-0.11} \text{ keV}$; there is some evidence for an additional low-temperature component as well.

The third softest spectrum belongs to one of the optically identified quasars (see §4.7), source 16 (CXOU J214016.05-230957.3). This source can be fit with a power-law of photon index $2.26^{+0.52}_{-0.25}$ or a MEKAL spectrum of $\text{kT}=1.2^{+0.59}_{-0.46} \text{ keV}$.

The hardest spectrum (with substantial counts) belongs to source C (CXOGLB J214022.92-231049.2), which we optically identify as a CV (§4.5). This source is fit with a power-law of photon index $1.46^{+0.31}_{-0.33}$, or a MEKAL spectrum of $\text{kT}=16^{+63}_{-11} \text{ keV}$. Both require enhanced N_H over the clus-

ter value; for the MEKAL spectrum this is $11^{+9}_{-6} \times 10^{20} \text{ cm}^{-2}$. This is consistent with its position in the X-ray color-color diagram, which suggests increased N_H .

Finally, source D (CXOU J214029.23-231031.3), while well-fit by a power-law of photon index $1.80^{+0.06}_{-0.06}$, is poorly fit by a single MEKAL spectrum ($\chi^2_{\nu} = 3.0$).

3.7. Unresolved Flux

Examination of Fig. 2 suggests a possible unresolved flux excess within the central region, e.g. within the dashed circle, which has a radius of $9'' = 5 r_c$. To investigate this, we computed the excess counts within $9''$ of the center of M30 by subtracting from the total counts within this circle the combination of the counts from all detected sources within their extraction regions, the estimated count contribution from PSF “spill” beyond the extraction regions, and the expected background counts. The resulting flux excess is 55 ± 10 counts (0.3–7 keV). This suggests that the presence of numerous additional faint sources below our detection limit of 4.5 counts. Assuming a luminosity function in the range observed for globular clusters by Pooley et al. (2002b), we find that the 55 excess counts within $9''$ indicate that 4–8 additional sources may be detected within this region by improving the detection limit by a factor of 2.5. One such faint source is the 4-count millisecond pulsar candidate suggested by Ransom et al. (2004), which lies just below our detection limit (see Fig. 2).

4. SEARCH FOR OPTICAL COUNTERPARTS

4.1. Astrometric Comparison

The center of M30 has been extensively imaged by the *HST* Wide-Field Planetary Camera 2 (WFPC2). Program GO-7379 (PI: Edmonds) has produced particularly deep, dithered imaging in F336W (*U*), F555W (*V*), and F814W (*I*). In order to effectively search for optical counterparts, it is necessary to establish a common astrometric zero point for the *Chandra* and *HST* datasets. While the images from both data sets contain World Coordinate System (WCS) solutions, the absolute accuracy of each of these is no better than about $0''.7$.

In order to establish a common zero point, we first determined an astrometric solution for a ground-based CTIO 1.5 m telescope *V*-band image of M30 (kindly provided by M. Bolte), relative to the *HST* Guide Star Catalog 2.2 astrometric system. We then selected secondary astrometric standards from the ground-based image and used these to obtain new astrometric solutions for each WFPC2 image that we used. This produced zero point shifts of about $0''.6$ relative to the *HST* WCS solutions given in the image headers. Curiously, we find a considerably larger shift for the relatively isolated “astrometric reference star” defined by Guhathakurta et al. (1998); our revised position for this star is:

$$\alpha = 21^{\text{h}} 40^{\text{m}} 22^{\text{s}} 29, \quad \delta = -23^{\circ} 10' 39''.6 \text{ (J2000)}. \quad (3)$$

This corresponds to shifts of $\Delta\alpha = -1''.5$ and $\Delta\delta = +2''.8$ relative to the position given by Guhathakurta et al. (1998). We note that the center position for M30 given by Sosin (1997), based on *HST* Faint Object Camera observations, differs from that of Guhathakurta et al. (1998) by similar shifts of $\Delta\alpha = -1''.1$ and $\Delta\delta = +2''.9$, even though the finding charts given in these two papers refer to nearly the same location on the sky. In comparing WFPC2 images of M30 from different epochs, we find that the apparent position of the astrometric star differs by up to about $0''.8$, which is within the expected

⁶ The NSATMOS model considers neutron star masses above a minimum mass of $0.5 M_{\odot}$.

TABLE 3
SPECTRAL FITS TO BRIGHTER M30 SOURCES

Source	ID	MEKAL					Power-law				
		kT (keV)	N_H (10^{20} cm $^{-2}$)	χ^2_ν/dof	F_X (10^{-15} cgs)	L_X (10^{31} cgs)	α	N_H (10^{20} cm $^{-2}$)	χ^2_ν/dof	F_X (10^{-15} cgs)	L_X (10^{31} cgs)
1	A2	$5.0^{+\infty}_{-1.2}$	$1.7^{+12.7}_{-0}$	1.24/5	5.8	5.6	$1.72^{+1.22}_{-0.53}$	$3.3^{+19.6}_{-1.6}$	1.20/5	6.1	5.9
2	A1	$0.51^{+0.04}_{-0.04}$	$5.2^{+0.9}_{-1.3}$	1.15/30	77.2	74.9	4.90	20.5	2.23/30	169	163
4	B	$5.0^{+12.8}_{-2.9}$	$5.4^{+7.8}_{-3.6}$	0.58/17	12.0	11.6	$1.80^{+0.62}_{-0.40}$	$8.7^{+11.3}_{-5.6}$	0.54/17	12.8	12.3
5	C	$16.5^{+63}_{-11.0}$	$10.9^{+9.4}_{-6.2}$	0.49/15	20.2	19.6	$1.46^{+0.31}_{-0.33}$	$13.2^{+11.0}_{-7.9}$	0.49/15	20.7	20.1
16	QSO	$1.21^{+0.59}_{-0.46}$	$1.7^{+3.4}_{-0}$	1.22/16	6.9	6.7	$2.26^{+0.52}_{-0.25}$	$1.8^{+5.8}_{-0.1}$	1.28/16	7.6	7.4
17	D	3.7	1.7	3.01/26	192	186	$1.80^{+0.06}_{-0.06}$	$1.7^{+0.5}_{-0}$	0.99/26	197	192
26		$4.5^{+2.1}_{-1.7}$	$5.6^{+4.8}_{-2.6}$	0.88/24	23.3	22.7	$1.84^{+0.33}_{-0.24}$	$8.5^{+6.2}_{-4.0}$	0.91/24	24.6	23.9
27	QSO	$5.1^{+25.9}_{-3.3}$	$2.1^{+5.8}_{-0.4}$	0.74/14	9.4	9.1	$1.80^{+0.67}_{-0.45}$	$4.8^{+9.3}_{-3.1}$	0.65/14	9.9	9.6
32		$3.3^{+4.9}_{-1.7}$	$1.7^{+2.2}_{-0}$	1.00/15	8.8	8.6	$1.90^{+0.39}_{-0.30}$	$1.7^{+3.8}_{-0}$	0.80/15	9.0	8.7
33		$3.6^{+2.0}_{-1.1}$	$1.7^{+0.6}_{-0}$	1.78/29	34.3	33.2	$1.81^{+0.17}_{-0.14}$	$1.7^{+1.8}_{-0}$	1.51/29	35.4	34.3
39 ^a	star	$0.71^{+0.13}_{-0.11}$	$0^{+6.7}_{-0}$	1.07/8	4.4	4.3	2.60	3.3	2.62/8	4.2	4.1
45		$4.0^{+7.4}_{-2.2}$	$2.2^{+8.6}_{-0.5}$	1.15/15	9.2	9.0	$1.85^{+0.66}_{-0.40}$	$4.6^{+10.7}_{-2.9}$	1.16/15	9.8	9.5

NOTE. — Spectral fits to cluster sources, with background subtraction, in XSPEC. Errors are 90% confidence for a single parameter; spectra are binned with 20 counts/bin for >500 counts, 10 counts/bin for >200 counts, 7 counts/bin for >100 counts, 5 counts/bin for sources with fewer counts. We do not calculate errors of fit parameters for poor quality ($\chi^2_\nu > 2.0$) fits. All fits include photoelectric absorption forced to be $\geq 1.7 \times 10^{20}$ cm $^{-2}$. X-ray fluxes in units of 10^{-15} erg s $^{-1}$ cm $^{-2}$. X-ray luminosities are in units of 10^{31} erg s $^{-1}$.

^aAcceptable fit requires a higher metallicity and lower N_H ; here we use solar metallicity.

uncertainty of the WFPC2 image header WCS solution zero points. Thus, it is not clear why the shift between the present results and those of Guhathakurta et al. (1998) is nearly 3'' in declination.

Following the completion of our astrometric analysis, we learned of an independent analysis by Ransom et al. (2004), which is based on the International Celestial Reference System (ICRS). These authors similarly find a substantial offset for the Guhathakurta et al. (1998) reference star. Ransom et al. (2004) report an absolute position for this star of $\alpha = 21^{\text{h}} 40^{\text{m}} 22^{\text{s}}.314$, $\delta = -23^\circ 10' 40''.10$ (J2000). Our position is offset from this by $\Delta\alpha = -0''.3$ and $\Delta\delta = +0''.5$. These offsets may largely represent the uncertainty in our astrometric solution for the CTIO 1.5 m frame, which is based on the *HST* Guide Star Catalog 2.2 astrometric system. Since we have applied a boresight correction to put the *Chandra* positions on our optical astrometric system, as described below, our astrometric comparison of *HST* and *Chandra* positions is not affected by any absolute offset of our astrometry from the ICRS.

We next turn to the astrometric alignment of the *Chandra* image. Source D, the brightest source in the *Chandra* field, is located 1'.6 east of the cluster center (see Fig. 1) and is on the WF3 chip of the GO-7379 dataset. There is a $V \approx 20$ star with a pronounced UV excess located within 0''.7 of the nominal *Chandra* position. Adopting this star as the likely optical counterpart to source D provides a boresight correction to the nominal *Chandra* positions of $\Delta\alpha = -0''.2$, $\Delta\delta = +0''.7$. Based on our subsequent identifications of counterparts to sources B and C, we judge the accuracy of this boresight correction to be about 0''.1 in each coordinate.

After applying this boresight correction to the *Chandra* detection positions, to put them on our optical astromet-

ric system, we searched the locations of the other *Chandra* sources in the *HST* frames. To facilitate this search in the crowded core region, we used the IRAF/STSDAS⁷ *drizzle* tool to reconstruct the Planetary Camera (PC) images from the GO-7379 dataset with $2\times$ oversampling, using the 12 separate dither positions for the *U*, *V*, and *I* filters. We combined all of the images for each filter at each position, using an exposure-weighted average. A portion of the resulting drizzle-reconstructed *U*-band image is shown in Fig. 9, with the cluster core radius and error circles for sources A1, A2, A3, B, and C overlaid. We also carried out a drizzle reconstruction of the entire WFPC2 fields for the GO-7379 dataset, after first using the IRAF/STSDAS *wmosaic* tool to combine the four separate WFPC2 frames into a single mosaic for each dither position and filter.

High quality photometry for M30 is available from several sources, including a *HST* WFPC2-based *UBV* analysis (Guhathakurta et al. 1998) and a ground-based *VI* analysis (Sandquist et al. 1999). While both photometry sets have proved useful in the search for optical counterparts, each has limitations. The ground-based photometry is most useful for the region outside of the half-mass radius, where image crowding is much less severe than within the central region. The Guhathakurta et al. (1998) analysis is based on the undithered GO-5324 dataset and thus does not reach as deep as is possible with the dithered GO-7379 dataset. Pietrukowicz & Kaluzny (2004) have analyzed the GO-7379 dataset to search for variable stars in M30, but have not published the detailed photometry. We found it useful to perform aperture

⁷ IRAF is distributed by NOAO, which is operated by AURA, under co-operative agreement with NSF. STSDAS is a product of the STScI, which is operated by AURA for NASA.

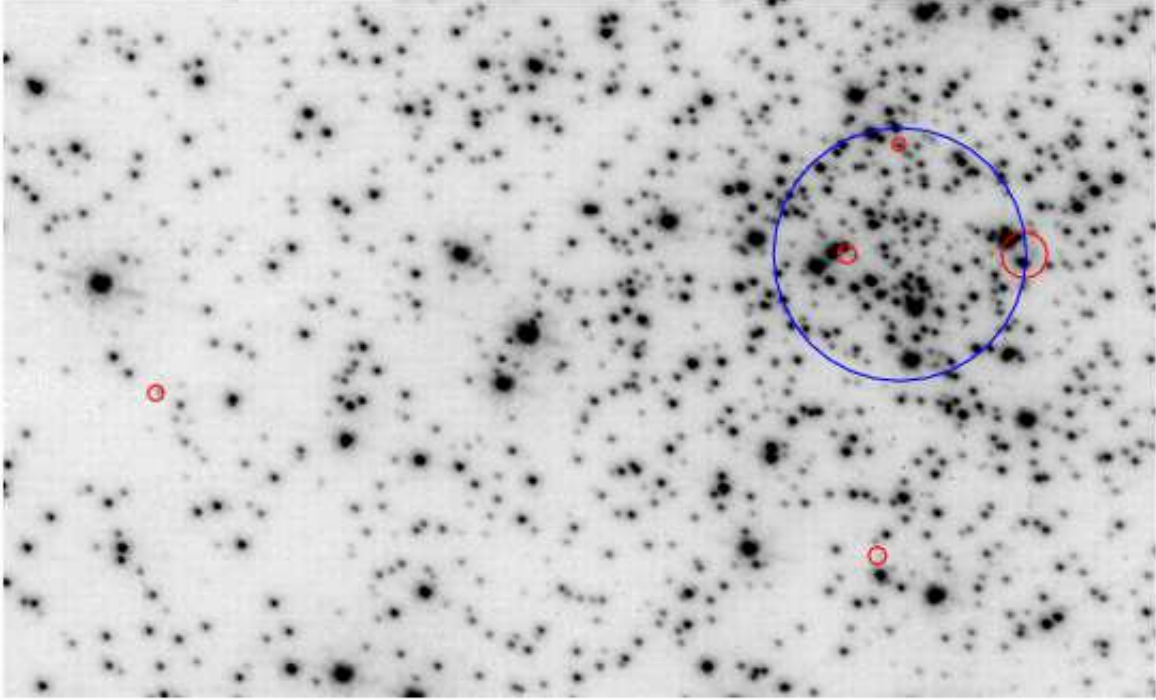


FIG. 9.— A $17'' \times 11''$ region of the drizzle-reconstructed U -band WFPC2 Planetary Camera image of M30. North is up and east is to the left. The core radius is indicated by the large circle in the northwest quadrant. Four-sigma X-ray error circles are indicated for sources A1, A2, A3, B, and C; see Fig. 2 for source map. (See the electronic edition of the *Journal* for a color version of this figure.)

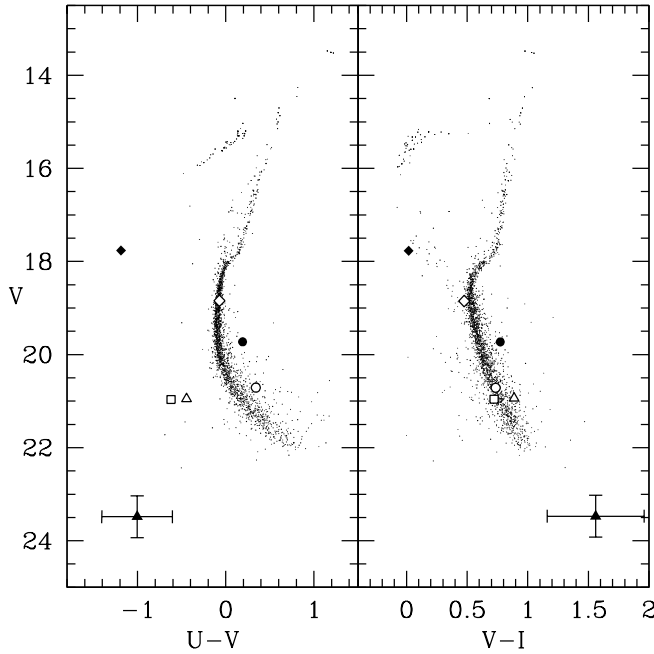


FIG. 10.— CMDs for the PC frames from aperture photometry of drizzled images. Points are plotted for stars detected in all three bands, U , V , and I . Chandra source candidate counterparts are indicated as follows: source A1—open diamond; source A2—solid diamond; source B—solid triangle with error bars; source C—open triangle; source D—square; source 7—open circle; source 10—solid circle. All objects lie in the PC field, except for source D (WF3) and source 10 (WF2).

photometry on the GO-7379 frames in order to obtain approximate results for a greater set of candidate counterparts than is available in the previously published photometry. Figure 10 shows the color-magnitude diagrams (CMDs) that result from

TABLE 4
CANDIDATE OPTICAL
COUNTERPART PHOTOMETRY

Object	U_{336}	V_{555}	I_{814}
A1	18.78	18.85	18.37
A2	16.58	17.77	17.75
B	22.5	23.5	21.9
C	20.50	20.94	20.05
D	20.34	20.96	20.24
7	21.05	20.71	19.98
10	19.92	19.73	18.95

our photometry for the PC field.

The photometry was performed on the drizzle-reconstructed U , V , and I frames, using a 4-pixel radius aperture, which corresponds to 2 PC pixels ($0''.09$). Stars were first detected in the U frame and then these positions were shifted to the V and I frames and recentered. Only those stars with locations within 0.5 pix of the mean shifts are included in these CMDs, in order to filter out stars for which blended images invalidate the aperture photometry. A few additional outliers were filtered out by rejecting stars that have brighter detected neighbors within $0''.22$. The magnitudes were transformed to the Johnson-Cousins system, using the calibrations given by Holtzman et al. (1995), with aperture corrections to a fiducial aperture of radius $0''.5$. Comparison of $(V, V-I)$ CMD with that of Sandquist et al. (1999) indicated very good agreement of the fiducial sequences, after additional offsets of $\Delta V = -0.1$ and $\Delta(V-I) = +0.1$ were applied to our magnitudes. A similar comparison of our $(V, U-V)$ CMD against that of Guhathakurta et al. (1998) similarly indicated very good agreement after applying an

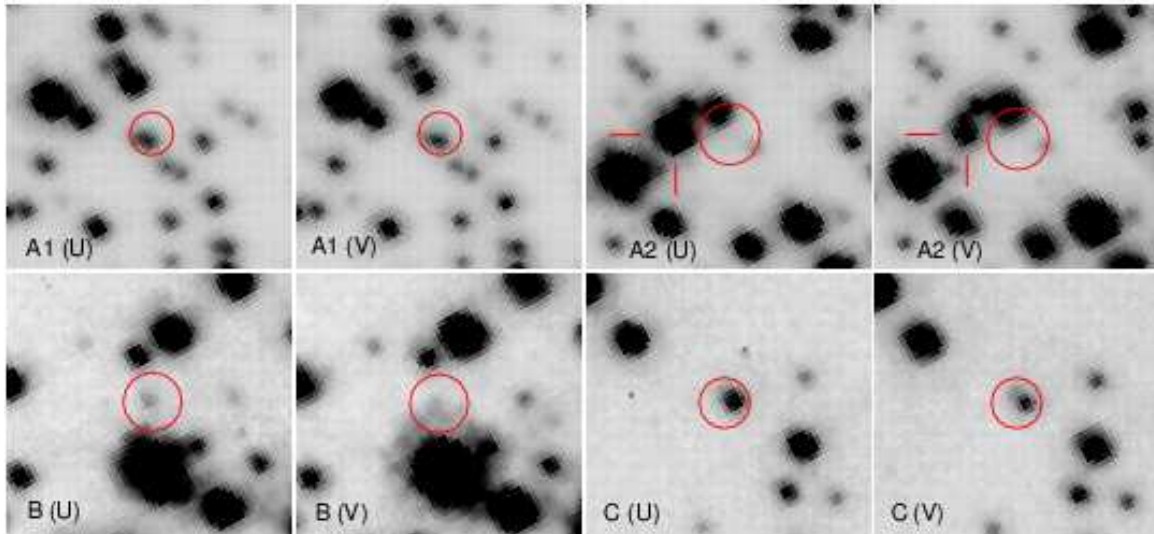


FIG. 11.— Finding charts for X-ray sources A1, A2, B, and C. North is up and east is to the left. Each chart is $1''.3$ in east-west dimension. For each source the left member of each chart pair shows the U -band image and the right member shows the V -band image. The error circles represent 4σ uncertainties in the boresight-corrected source positions. The lines in the A2 charts indicate the extremely blue star that lies just outside of the error circle. (See the electronic edition of the Journal for a color version of this figure.)

offset of $\Delta(U-V) = -0.3$. (We note that they used transformations based on U , B , and V magnitudes, while we only had U and V magnitudes available.) These offsets have been adopted in the photometric results reported below. It can be seen, from Fig. 10, that the CMDs produced by this aperture photometry process show well-defined sequences to the detection limit (defined by the U -band image) of about 3 magnitudes below the main-sequence turnoff (MSTO). We also performed aperture photometry on the mosaics, to determine magnitudes for the objects that lie in the Wide Field (WF) images, and determined the zeropoint shifts between WF and PC photometry.

Table 1 lists the optical counterparts that were found. The sources A1, A2, B, and C, 7, and 10 all have possible counterparts based on positional agreement and optical photometry. The photometry for the counterparts is summarized in Table 4 and is plotted in Fig. 10. The positions of the A1, B, C, 7, and 10 counterparts agree to within about $0''.05$ with the boresight-corrected *Chandra* positions. In the following, we discuss the nature of each of these counterparts as well as likely counterparts to source D and a few additional sources. Figure 11 shows U - and V -band finding charts, from the drizzle-reconstructed images, for the candidate counterparts to sources A1, A2, B, and C. Figure 12 shows V -band finding charts for the remaining sources within r_h and source D.

4.2. Source A1

Examination of the drizzle-reconstructed images indicates that there is a pair of stars with a separation of only about $0''.03$ within $0''.05$ of the position of source A1, the likely qLMXB. The combined photometry for the two stars falls on the main sequence in the $(V, U-V)$ CMD and to the blue side of the MSTO region in the $(V, V-I)$ CMD, as shown in Fig. 10. The combined magnitude of the two stars is $V = 18.9$. Since the fainter (easternmost) of the two stars appears somewhat bluer than the brighter star (see Fig. 11), it must lie somewhat to the blue side of the MSTO, making it more likely to be the counterpart than the brighter, redder star. We estimate that this potential counterpart has $V \gtrsim 20$, corresponding to $M_V \gtrsim 5$. By comparison, Edmonds et al. (2002) have identified an optical counterpart to the qLMXB X5 in 47 Tuc with

$M_V = 8.1$, noting that two other identified qLMXB counterparts have similar absolute magnitudes of $M_V \sim 8$. Given that the candidate counterpart may be 3 mag brighter than this, it is quite possible that this represents a case of random positional coincidence in the extremely crowded core region and that neither of the two stars in the source A1 error circle is the true optical counterpart to the qLMXB.

4.3. Source A2

As noted in §3.2, A2 is only detected by WAVDETECT in a high-energy band (2.5–7 keV), but is detected by PWDETECT in broad-band images. In order to better isolate A2 from its brighter, softer neighbor A1, we used the CIAO DMSTAT task to find the centroid of the events within a $1''$ radius circular aperture about the apparent A2 source location using a range of low-energy cutoff values; a uniform upper cutoff of 6 keV was adopted. As the low-energy cutoff was increased from 0.5 to 2.0 keV, the centroid shifted by $0''.2$. The formal error in the centroid is about $0''.07$ in each coordinate. The range of centroided positions for A2 is offset by $0''.1 - 0''.3$ from an extremely blue star, with the smaller offset corresponding to the low-energy cutoff values in excess of 1.75 keV. The star is denoted as #3327 in the photometry of Guhathakurta et al. (1998); they find $V = 17.84$, $B-V = -0.17$, and $U-V = -1.07$. Our aperture photometry similarly gives $V = 17.77$, $U-V = -1.19$, and $V-I = 0.02$. In the $(V, V-I)$ CMD, this star is as blue as the blue tip of the horizontal branch, which represents the bluest color possible for a black body. Its position in this CMD is consistent with the blue straggler region. However, its $U-V$ color is over 1 mag bluer than the blue stragglers, which lie vertically above the MSTO in the $(V, U-V)$ CMD. Not surprisingly, this star is the brightest object in the cluster core in *HST* WFPC2 imaging in the F160W ultraviolet filter. Given the extreme colors of this star and its possible positional consistency with A2, further investigation of it as a possible counterpart is appropriate.

The optical color indices of the possible A2 counterpart are consistent with an early B spectral type ($\sim B2$) and its absolute magnitude of $M_V = 3.1$ is within the observed range for subdwarf B (sdB) stars (Edelmann et al. 2003). Common envelope evolution in a close binary system is a likely scenario

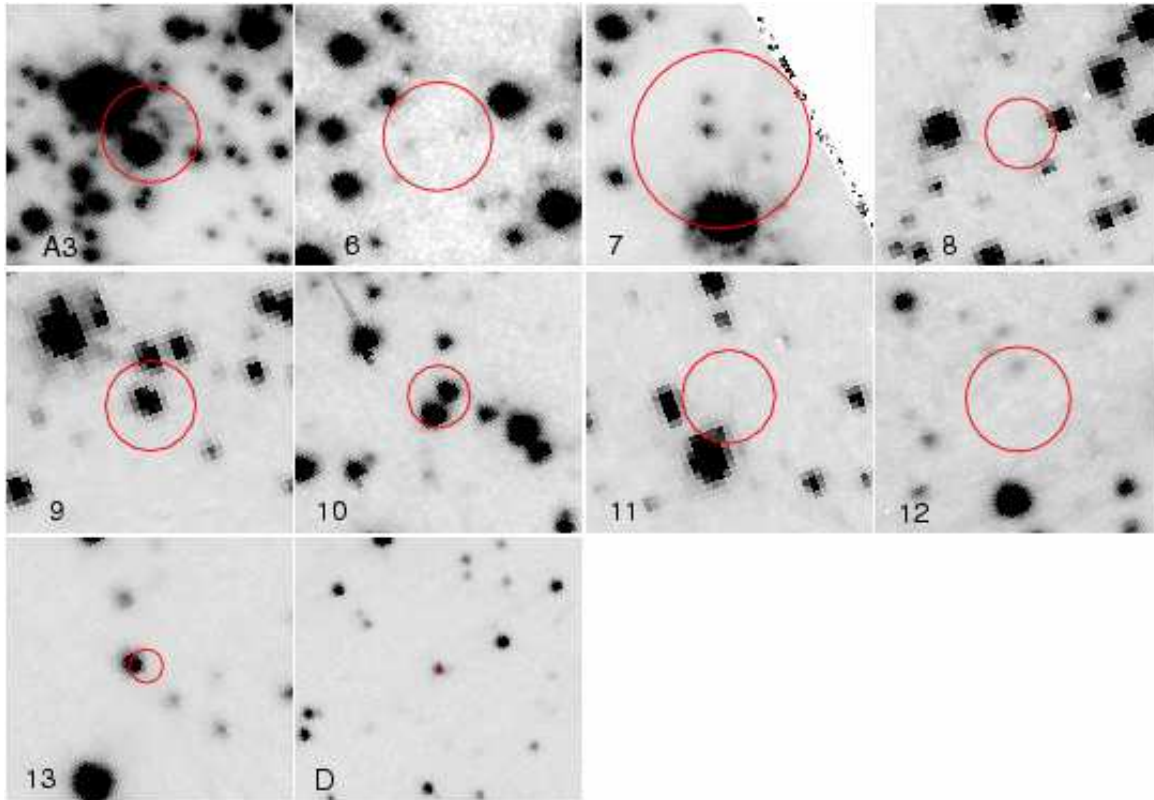


FIG. 12.— V-band finding charts for remaining X-ray sources within the half-mass radius and source D, which defines the boresight correction. North is up and east is to the left. The east-west dimensions are as follows: $2''$ (sources A3, 6, 7); $4''$ (sources 8–13); $8''$ (source D). The error circles represent 4σ uncertainties in the boresight-corrected source positions. (See the electronic edition of the *Journal* for a color version of this figure.)

for the formation of these extreme horizontal branch (EHB) and post-EHB stars (Han et al. 2002, 2003). This is supported by the observation that a substantial fraction ($69 \pm 9\%$) of sdB stars appear to be in close binary systems (Maxted et al. 2001). The shortest observed orbital period to date is 1.8 h (Maxted et al. 2002). The binary companion of the sdB star is likely to be a white dwarf in many cases (e.g. Napiwotzki et al. 2001; Maxted et al. 2002). X-ray emission has been observed from some subdwarf binaries (e.g. Israel et al. 1997), although this does not appear to be a common type of source. Thus, it appears likely that the near positional coincidence between A2 and the sdB star represents a chance superposition. We note that no object with similar optical properties is observed as a counterpart to a *Chandra* source in either of the two well-studied clusters 47 Tuc (Edmonds et al. 2003) and NGC 6397 (Taylor et al. 2005). Nevertheless, *Chandra* source A2 is clearly a cluster member given its location within $1''$ of the cluster center. As noted in §3.3, it has X-ray color indices consistent with the likely CVs, sources B and C, which suggests that source A2 is also likely to be a CV with a faint optical counterpart. The extremely crowded region about the position of A2 might well preclude the optical detection of such a CV, even with relatively deep *HST* imaging.

4.4. Source B

Source B is closely aligned with a faint object that is visible in the GO-7379 *U* frame. In the *V* and *I* frames, it lies in the halo of a giant-branch neighbor, at a separation of just $0''.35$. In order to better estimate its *V* and *I* magnitudes, we carried out PSF subtraction using DAOPHOT, defining the PSF from nearby stars of comparable brightness to the neighbor. Given the $\Delta V \approx 7$ difference between the source B counterpart and its neighbor, this results in large uncertainties in the

magnitudes; we estimate these as 0.2 mag for *U* and *I* and 0.4 mag in *V*. The resulting magnitudes and colors are $V = 23.5$ ($M_V = 8.6$), $U - V = -1.0$, and $V - I = 1.7$. We have plotted the corresponding location of the source B counterpart, with error bars, in Fig. 10. While the $V - I$ color is consistent with a faint main sequence location, there is a very large apparent UV excess relative to an extension of lower main sequence. These photometric properties are consistent with a CV interpretation, in which the *V* and *I* bands are strongly dominated by radiation from the secondary, while the *U* band is dominated by contributions from the much hotter white dwarf and accretion disk (c.f. Edmonds et al. 2003). Aperture photometry of the combined *U* frames for each of the 12 dither positions suggests substantial time variability. Based on these optical properties of its apparent counterpart, its location within $5''$ of the cluster center, and the consistency of the X-ray colors of sources B and C, it appears likely that source B is a CV located near the core of M30.

4.5. Source C

Source C is closely aligned with an object located $12''$ from the cluster center with $V = 20.94$ ($M_V = 6.1$), $U - V = -0.44$, and $V - I = 0.89$. While the $V - I$ color is just to the red of the main sequence, the $U - V$ color is 0.6 mag to the blue of the main sequence (see Fig. 10). As for source B, this is entirely consistent with a CV interpretation. Curiously, this counterpart does not appear in the Guhathakurta et al. (1998) photometry, although other nearby stars of similar magnitude are detected. A check of the GO-5324 F336W image, on which the Guhathakurta et al. (1998) photometry is based, indicates that this candidate counterpart to source C is present, but is located within 3 pixels of the vignetted region of the PC field. This may account for it being excluded from the final pho-

tometry list. This object is well detected in the single 600 s F336W exposure from GO-5603 (obtained in 1994). Approximate aperture photometry indicates that the object is about 1.0 mag fainter in F336W, in 1999 versus 1994. This high level of variability provides additional support for the CV interpretation.

4.6. Source D

As previously mentioned, our boresight correction is defined by source D. The likely counterpart has $V = 20.74$, a $V-I$ color consistent with the main sequence and a $U-V$ color that is 0.6 mag to the blue of the main sequence. Thus, its photometric properties appear quite similar to those of source C, as can be seen in Fig. 10. This argues for interpreting source D as a CV in M30, which would be quite interesting given its location at $1.4 r_h$. However, the inferred $L_X = 2 \times 10^{33} \text{ erg s}^{-1}$ for source D would put it among the most luminous CVs seen in any globular cluster. In addition, its *Chandra* spectrum, discussed in §3.6.2 above, is not well fit by a MEKAL spectrum, unlike those of sources A2, B, and C.

In order to obtain further information on the source D counterpart, we obtained optical spectra using the Hydra spectrographs on the CTIO 4 m telescope in 2003 July and on the WIYN 3.5 m telescope in 2003 September. The seeing was poor throughout the CTIO run, typically exceeding $2''.5$. Thus, the light of this object was strongly mixed with that of its much brighter neighbor at $2''$ separation and only a combined spectrum was obtained. While the seeing at WIYN was generally better, the large airmass of this southern cluster resulted in a similar mixing of the star with its neighbor. Examination of this combined spectrum indicates a emission line at 5562 \AA with a FWHM of $\sim 12 \text{ \AA}$, with no evidence for Balmer emission at the cluster velocity. While the detection of only one emission line precludes a definitive redshift determination, we note that identifying this as the relatively isolated Mg II $\lambda 2800$ line would imply a redshift of $z = 0.99$. A long-slit spectrum of the optical counterpart to source D would greatly assist in determining its physical nature.

4.7. Other Identifications

Two additional sources visible in Fig. 2, source 6 (CXOGLB J214021.48-231054.5) and source 7 (CXOGLB J214021.56-231032.6), fall within the drizzled Planetary Camera field. No object is detected in the U -band image within the error circle for source 6, while there are two very faint stars within the error circles in the V - and I -band images (see Fig. 12). Source 7 is very close to the edge of the PC field and was imaged in 8 of 12 pointings. Three faint objects are detected within the error circles in all three bands for source 7 and one additional faint object is detected in the V and I bands (see Fig. 12). None of these objects appears to be blue. Photometry for the brightest of the three is shown in Fig. 10. While this object lies on the main sequence in the $(V, V-I)$ CMD, it has an apparent UV deficit and is thus not likely to be a CV. We note that active binary (AB) counterparts to *Chandra* sources in globular clusters typically lie on the main sequence or somewhat above it, as seen in the clusters NGC 6397 (Grindlay et al. 2001b), NGC 6752 (Pooley et al. 2002a), 47 Tuc (Edmonds et al. 2003), and M4 (Bassa et al. 2004). Thus, the CMD location of this possible counterpart to source 7 is consistent with an active binary interpretation.

It can be seen in Fig. 12 that optical objects are detected in several of the source error circles in the WF fields. The

source 9 error circle contains a close pair of objects. This location has only been imaged by the GO-5630 program, which provides F555W (V) and F160BW coverage. The images in the latter band are rather shallow. Since the possible source 9 counterparts are only detected in F555W, no color information is available. Of the two objects in the source 10 error circle, the southern object lies on the main sequence in both CMDs, while the northern object lies above the main sequence in both CMDs (see Fig. 10). Thus, this latter object is consistent with being an active binary. The faint object detected near the edge of the source 12 error circle in the V and I frames is not detected in the U frame. It is thus likely to be a faint main sequence star. The object detected on the edge of the error circle for source 13 lies on the main sequence in both CMDs. Thus, this object does not appear likely to be the source 13 counterpart, despite its close proximity to the source 13 location.

We attempted to determine optical counterparts for additional *Chandra* sources listed in Table 1, by comparison of the *Chandra*, *HST*, and ground-based images, and then obtaining Hydra spectroscopy for candidate counterparts. As noted above, the crowded conditions, even outside of the half-mass radius, proved challenging for the spectroscopic program. At both CTIO and WIYN, the minimum fiber size is $2''$. The goal of this effort was to determine whether any other *Chandra* sources are likely to be associated with cluster objects, particularly for sources, such as D, that lie beyond the half-mass radius. Any source in the cluster halo that is confirmed as a cluster member is a good candidate for having been ejected from the cluster core by an energetic binary interaction.

Chandra source 39 (CXOU J214033.30-231236.3) at $3.2'$ from the cluster center coincides with a bright star that is almost certainly a foreground object. This star is listed as #1 in the photometry of Sandquist et al. (1999) and has $V = 12.03$, $V-I = 0.80$, which place it at the magnitude level of the tip of the giant branch but 0.6 mag bluer in $V-I$ color. The color index indicates a spectral type of approximately G2. The X-ray to optical flux ratio of $F_X/F_V \approx 10^{-4}$ is within the range observed for main-sequence early G stars (Huensch et al. 1998). The soft X-ray spectrum of this source provides additional evidence that it is a foreground star (see §3.6.2).

The CTIO and WIYN Hydra spectroscopy described previously resulted in the tentative identification of three of the other *Chandra* sources, numbers 16, 27, and 50 in Table 1 (CXOU J214016.05-230957.3, 214015.01-231217.5, and 214037.03-231337.1, respectively). These objects are located at distances of $1.6'$, $2.2'$, and $4.4'$ respectively, from the cluster center. While the spectra of the apparent counterparts to sources 16 and 27 are blended with neighboring stars, there are broad emission lines apparent in each of the spectra that give consistent redshifts. These lines are enhanced when a smooth continuum is fit and subtracted. For source 16, Ly- α , C IV $\lambda 1549$, and C III] $\lambda 1909$ give a mean redshift of 2.42. For source 27, Ly- α , N V $\lambda 1240$, Si IV+O IV] $\lambda 1400$, and C IV $\lambda 1549$ give a mean redshift of 3.08. Source 50 is positionally coincident with an apparent elliptical galaxy with a redshift of 0.27, based on a detection of the Mg b triplet and the Ca II H & K break. It is not surprising that these three sources, which all lie well outside of the cluster half-mass radius, are background objects. However, this does not resolve the issue of whether a small number of the other sources near or outside of r_h may actually be cluster members that were ejected from the central region. This will require additional spectroscopy, under more favorable observing conditions. The use of a long slit or slitlets would facilitate separation of objects from close

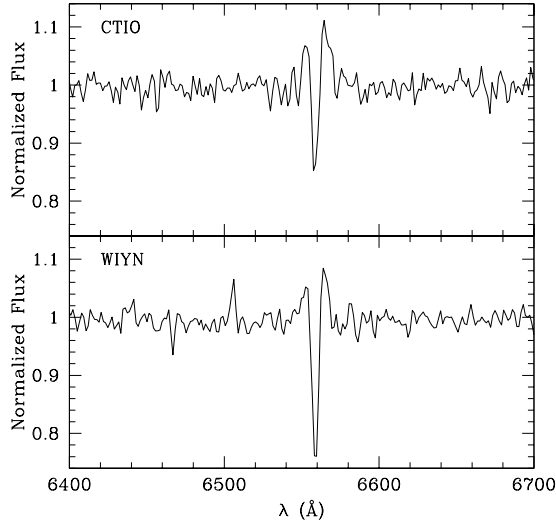


FIG. 13.— $H\alpha$ line profiles from Hydra multiobject spectroscopy of possible counterpart to *Chandra* source 36. The CTIO spectrum (top) was obtained in 2003 July; the WIYN spectrum (bottom) was obtained in 2003 September. The flux has been normalized to the continuum in both cases. Note the apparent blue and red emission wings about $H\alpha$, which suggest the superposition of a broad emission feature on a narrower absorption line. The apparent weak emission feature near 6505 Å in the WIYN spectrum is likely noise, given its absence in the CTIO spectrum.

neighbors.

In addition to the tentative identifications just described, source 40 (CXOU J214008.37-231118.9) lies within about $1''$ of a $V = 16.4$ star, located at $3\frac{1}{2}$ from the cluster center, that lies about 0.06 mag to the blue of the ridgeline of the giant branch in the $(V, V-I)$ CMD of Sandquist et al. (1999). This star is also detected by Richer et al. (1988) with nearly the same V magnitude ($V = 16.5$) and a $B-V$ color that is about 0.08 mag to the blue of the giant branch in the $(V, B-V)$ CMD. Examination of the object in deep B , V , and I CTIO 1.5 m images (kindly provided by M. Bolte) indicates an elongation to the northeast that becomes more prominent at shorter wavelength. This suggests that the optical object may be the superposition of a faint blue star with a much brighter giant. The separation between the two apparent objects is of order $0''.5$. The spectra for the combined object, obtained at both CTIO and WIYN, show definite emission components in the red and blue wings of the $H\alpha$ absorption line, as can be seen in Figure 13. This suggests that the putative blue object has a broad single-component $H\alpha$ emission feature that overlies the absorption line of the giant. Given the small offset between this apparent emission object and the much brighter giant, further spectroscopic study will require high angular resolution. If a broad $H\alpha$ emission feature at a velocity consistent with cluster membership were confirmed, then source 40 may be consistent with being a CV that was ejected from the cluster core.

We checked the positions of the eight variable stars that were identified by Pietrukowicz & Kaluzny (2004) within the GO-7379 field. We find that none of these stars is positionally coincident with a *Chandra* source.

5. DISCUSSION

It is interesting to ask whether the observed size of the X-ray source population in M30 accords with expectation. Pooley et al. (2003) have shown that for 12 globular clusters observed by *Chandra*, the X-ray source population size scales

approximately linearly with the predicted stellar encounter rate. They interpret this as strong empirical evidence that the long-observed overabundance of exotic binaries in clusters is primarily the result of dynamical formation in the dense core regions. Following Verbunt & Hut (1987), they define a normalized encounter rate Γ as the volume integral to the half-mass radius of ρ^2/v , where ρ is the total mass density, v is the velocity dispersion, and single-mass King (1966) model structure is adopted for the radial profiles of ρ and v . Most of the contribution to Γ comes from the core and the immediately surrounding region; a simple computation using an analytic King model shows that about 90% of the interactions occur within $2r_c$. As noted by Pooley et al. (2003), this formalism leads to the scaling $\Gamma \propto \rho_0^2 r_c^3 / v_0$.

M30 is one of the clusters included in the Pooley et al. (2003) sample and their estimate of its background-corrected population size of ~ 5 – 6 *Chandra* sources within the half-mass radius agrees well with their prediction of ~ 5 sources from their empirical N – Γ relation. Our estimate of the background-corrected source population size is twice as large, at 10 ± 2 , where the error represents the uncertainty in the background correction only, as do the error bars in Fig. 2 of Pooley et al. (2003). Our background-corrected source count suggests that M30 has a source excess relative to its computed interaction rate Γ , although small number statistics are clearly an issue here.

Somewhat surprisingly, M30 has the fourth smallest interaction rate in the Pooley et al. (2003) sample, notwithstanding its very high central density. This is a consequence of its small core size. Pooley et al. (2003) adopted values of core radius, central density, and central velocity dispersion from the Harris (1996) compilation (2003 February online version); the values for M30 are $r_c = 3''.6$ and $\rho_0 = 1.1 \times 10^5 M_\odot \text{pc}^{-3}$. We note that given the collapsed-core status of M30, these values are rather uncertain. Sosin (1997) has placed an upper limit of $1''.9$ on the core radius, suggesting a preferred value of $1''$, and has estimated a central density of $8.5 \times 10^5 M_\odot \text{pc}^{-3}$ from dynamical modeling. These large changes in r_c and ρ_0 produce partially compensating changes in the value of Γ , increasing it by a factor of 1.3 for v_0 held fixed and by a factor of 1.7 for $v_0 \propto \rho_0^{0.5} r_c$ (as for a King model). Another source of uncertainty is that a single-mass King model does not give a good description of the collapsed-core structure of M30. It is interesting to note that another of the three core-collapsed clusters in the Pooley et al. (2003) sample, NGC 6397, significantly deviates from the empirical N – Γ relation in the sense of having an overabundance of X-ray sources relative to the encounter rate computed from the Harris (1996) values of core parameters, including a core radius of $3''$. We note that even with an HST-based analysis of the star count profile of NGC 6397, the core radius value remains uncertain. Taylor et al. (2005) find a best fit value of $4''.4 \pm 3''.2$ ($1\text{-}\sigma$ errors). This uncertainty range leads to a corresponding uncertainty in Γ , since $\Gamma \propto r_c$ if the central surface brightness and central velocity dispersion are fixed.

Given the uncertainties arising from the core-collapsed status of M30 and its consequently small core size, we suggest that its relation to the other clusters in the Pooley et al. (2003) sample is not entirely clear. Simple models for core collapse produce the scalings $\rho_0 \propto r_c^{-2.2}$ and $v_0 \propto r_c^{-0.05}$ Cohn (1980). These result in $\Gamma \propto r_c^{-1.4}$, indicating that clusters undergoing core radius oscillations should experience episodic bursts of strongly enhanced binary formation and ejection as the core

passes through its densest phases. Thus, the size of the X-ray binary population in a collapsed-core cluster may undergo substantial fluctuations in time. In light of these issues, detailed dynamical simulations of the evolution of binary populations in clusters undergoing core collapse would be very helpful.

6. SUMMARY

Our *Chandra* ACIS-S imaging of the collapsed-core globular cluster M30 has detected a centrally concentrated population of X-ray sources, including six within $12''$ of the cluster center and three within the $1''.9$ core radius. There is a net excess of about 10 sources above background within the half-mass radius. The brightest core source (A1) has an X-ray flux and spectrum that are both consistent with it being a qLMXB. The other central sources (A2, A3, B, and C) all have X-ray properties consistent with being CVs. We have identified likely optical counterparts to sources B and C that are similarly consistent with a CV interpretation. While we have suggested possible counterparts to sources A1 and A2, the status of these is uncertain and will require further investigation. Sources 7 and 10, which lie at $17''$ and $51''$ from the cluster center, respectively, have possible active binary counterparts. There remains a possibility of a significant number of additional faint sources in and near the core that lie somewhat below our detection limit of about 4.5 counts (corresponding to a source luminosity of $\sim 4 \times 10^{30}$ erg s $^{-1}$). Additional *Chandra* imaging would be very useful in searching for a fainter source population.

Our analysis of the radial distribution of the sources suggests that those belonging to the cluster are largely confined to the half-mass radius. There is some evidence for a small excess of sources over the expected background between r_h and $2r_h$; some of these may have been ejected from the central regions. The radial profile of the sources within r_h implies a typical source mass of about $1.3 \pm 0.2 M_\odot$, which is consistent with a variety of binary systems, including CVs.

Our analysis of the X-ray spectrum of source A1 indicates that it is best fit by a model for a neutron star thermally radiating through a hydrogen atmosphere, consistent with the

qLMXB interpretation. While the spectral modeling does not provide tight constraints on the neutron star mass and radius, it does demonstrate consistency with standard neutron star structure models.

Our effort to identify additional sources using ground-based optical spectroscopy with the CTIO and WIYN Hydra multiobject spectrographs demonstrated that two of the sources beyond the half-mass radius are quasars. The optical spectrum of source D, the brightest source in the field, shows no evidence for H α emission, while it does show a possible redshifted emission line. Thus it is more likely consistent with a background AGN than with a cluster CV. The spectroscopy did identify an object, also located beyond the half-mass radius, that shows H α emission wings about an absorption line. This object appears to be the superposition of two stars that are not well resolved by ground-based imaging and are outside of the field of HST imaging. Further investigation of this intriguing object is clearly warranted.

The core-collapsed status of M30 complicates a comparison of its *Chandra* source population size N with the empirical relation between N and collision rate Γ established for other clusters. While the observed population of about 10 sources above background within the half-mass radius is twice as large as the prediction of the relation, the determination of an appropriate Γ value for M30 is challenging given its very small core size and strong deviation from King-model structure in the inner region. A deeper X-ray luminosity function and detailed modeling of source population evolution in a collapsed-core cluster would facilitate further investigation of this issue.

We are grateful to Mike Bolte and Ron Gilliland for graciously providing ground-based images of M30 for our study. We thank Xavier Koenig and Allen Rogel for obtaining Hydra spectra of candidate source counterparts. We also appreciate the helpful suggestions of the referee.

This project was supported by NASA *Chandra* grant GO2-3037X to Indiana University.

REFERENCES

- Bassa, C., Pooley, D., Homer, L., Verbunt, F., Gaensler, B. M., Lewin, W. H. G., Anderson, S. F., Margon, B., Kaspi, V. M., & van der Klis, M. 2004, *ApJ*, 609, 755
- Bergbusch, P. A., & Vandenberg, D. A. 1992, *ApJS*, 81, 163
- Brandt, W. N., & Hasinger, G. 2005, *ARA&A*, 43, 827
- Broos, P., Townsley, L., Getman, K., & Bauer, F. 2002, ACIS Extract, An ACIS Point Source Extraction Package, Pennsylvania State University, http://www.astro.psu.edu/xray/docs/TARA/ae_users_guide.html
- Brown, E. F., Bildsten, L., & Rutledge, R. E. 1998, *ApJ*, 504, L95
- Campana, S., Colpi, M., Mereghetti, S., Stella, L., & Tavani, M. 1998, *A&A Rev.*, 8, 279
- Carney, B. W. 1996, *PASP*, 108, 900
- Carretta, E., Gratton, R. G., Clementini, G., & Fusi Pecci, F. 2000, *ApJ*, 533, 215
- Cohn, H. 1980, *ApJ*, 242, 765
- Cohn, H. 1985, in *IAU Symp. 113: Dynamics of Star Clusters*, 161–177
- Damiani, F., Maggio, A., Micela, G., & Sciortino, S. 1997, *ApJ*, 483, 370
- Davis, J. E. 2001, *ApJ*, 562, 575
- Djorgovski, S., & King, I. R. 1986, *ApJ*, 305, L61
- Edelmann, H., Heber, U., Hagen, H.-J., Lemke, M., Dreizler, S., Napiwotzki, R., & Engels, D. 2003, *A&A*, 400, 939
- Edmonds, P. D., Gilliland, R. L., Heinke, C. O., & Grindlay, J. E. 2003, *ApJ*, 596, 1177
- Edmonds, P. D., Heinke, C. O., Grindlay, J. E., & Gilliland, R. L. 2002, *ApJ*, 564, L17
- Feigelson, E. D., Broos, P., Gaffney, J. A., Garmire, G., Hillenbrand, L. A., Pravdo, S. H., Townsley, L., & Tsuboi, Y. 2002, *ApJ*, 574, 258
- Freeman, P. E., Kashyap, V., Rosner, R., & Lamb, D. Q. 2002, *ApJS*, 138, 185
- Gendre, B., Barret, D., & Webb, N. A. 2003, *A&A*, 400, 521
- Giacconi, R., Rosati, P., Tozzi, P., & et al. 2001, *ApJ*, 551, 624
- Grindlay, J. E., Camilo, F., Heinke, C. O., Edmonds, P. D., Cohn, H., & Lugger, P. 2002, *ApJ*, 581, 470
- Grindlay, J. E., Heinke, C., Edmonds, P. D., & Murray, S. S. 2001a, *Science*, 292, 2290
- Grindlay, J. E., Heinke, C. O., Edmonds, P. D., Murray, S. S., & Cool, A. M. 2001b, *ApJ*, 563, L53
- Guhathakurta, P., Webster, Z. T., Yanny, B., Schneider, D. P., & Bahcall, J. N. 1998, *AJ*, 116, 1757
- Han, Z., Podsiadlowski, P., Maxted, P. F. L., & Marsh, T. R. 2003, *MNRAS*, 341, 669
- Han, Z., Podsiadlowski, P., Maxted, P. F. L., Marsh, T. R., & Ivanova, N. 2002, *MNRAS*, 336, 449
- Harris, W. E. 1996, *AJ*, 112, 1487
- Heinke, C. O., Grindlay, J. E., Edmonds, P. D., Cohn, H. N., Lugger, P. M., Camilo, F., Bogdanov, S., & Freire, P. C. 2005, *ApJ*, 625, 796
- Heinke, C. O., Grindlay, J. E., Edmonds, P. D., Lloyd, D. A., Murray, S. S., Cohn, H. N., & Lugger, P. M. 2003a, *ApJ*, 598, 516
- Heinke, C. O., Grindlay, J. E., Lloyd, D. A., & Edmonds, P. D. 2003b, *ApJ*, 588, 452

- Heinke, C. O., Grindlay, J. E., Lugger, P. M., Cohn, H. N., Edmonds, P. D., Lloyd, D. A., & Cool, A. M. 2003c, *ApJ*, 598, 501
- Holtzman, J. A., Burrows, C. J., Casertano, S., Hester, J. J., Trauger, J. T., Watson, A. M., & Worthey, G. 1995, *PASP*, 107, 1065
- Howell, J. H., Guhathakurta, P., & Tan, A. 2000, *AJ*, 119, 1259
- Huensch, M., Schmitt, J. H. M. M., & Voges, W. 1998, *A&AS*, 132, 155
- Hut, P., McMillan, S., Goodman, J., Mateo, M., Phinney, E. S., Pryor, C., Richer, H. B., Verbunt, F., & Weinberg, M. 1992, *PASP*, 104, 981
- in't Zand, J. J. M., van Kerkwijk, M. H., Pooley, D., Verbunt, F., Wijnands, R., & Lewin, W. H. G. 2001, *ApJ*, 563, L41
- Israel, G. L., Stella, L., Angelini, L., White, N. E., Kallman, T. R., Giommi, P., & Treves, A. 1997, *ApJ*, 474, L53+
- Johnston, H. M., Verbunt, F., & Hasinger, G. 1994, *A&A*, 289, 763
- Kim, D.-W., Cameron, R. A., Drake, J. J., Evans, N. R., Freeman, P., Gaetz, T. J., Ghosh, H., Green, P. J., Harnden, Jr., F. R., Karovska, M., Kashyap, V., Maksym, P. W., Ratzlaff, P. W., Schlegel, E. M., Silverman, J. D., Tananbaum, H. D., Vikhlinin, A. A., Wilkes, B. J., & Grimes, J. P. 2004, *ApJS*, 150, 19
- King, I. R. 1966, *AJ*, 71, 64
- Lugger, P. M., Cohn, H. N., & Grindlay, J. E. 1995, *ApJ*, 439, 191
- Maxted, P. f. L., Heber, U., Marsh, T. R., & North, R. C. 2001, *MNRAS*, 326, 1391
- Maxted, P. F. L., Marsh, T. R., Heber, U., Morales-Rueda, L., North, R. C., & Lawson, W. A. 2002, *MNRAS*, 333, 231
- Napiwotzki, R., Edelmann, H., Heber, U., Karl, C., Drechsel, H., Pauli, E.-M., & Christlieb, N. 2001, *A&A*, 378, L17
- Phillips, K. J. H., Mewe, R., Harra-Murnion, L. K., Kaastra, J. S., Beiersdorfer, P., Brown, G. V., & Liedahl, D. A. 1999, *A&AS*, 138, 381
- Pietrukowicz, P., & Kaluzny, J. 2004, *Acta Astronomica*, 54, 19
- Pooley, D., Lewin, W. H. G., Anderson, S. F., Baumgardt, H., Filippenko, A. V., Gaensler, B. M., Homer, L., Hut, P., Kaspi, V. M., Makino, J., Margon, B., McMillan, S., Portegies Zwart, S., van der Klis, M., & Verbunt, F. 2003, *ApJ*, 591, L131
- Pooley, D., Lewin, W. H. G., Homer, L., Verbunt, F., Anderson, S. F., Gaensler, B. M., Margon, B., Miller, J. M., Fox, D. W., Kaspi, V. M., & van der Klis, M. 2002a, *ApJ*, 569, 405
- Pooley, D., Lewin, W. H. G., Verbunt, F., Homer, L., Margon, B., Gaensler, B. M., Kaspi, V. M., Miller, J. M., Fox, D. W., & van der Klis, M. 2002b, *ApJ*, 573, 184
- Rajagopal, M., & Romani, R. W. 1996, *ApJ*, 461, 327
- Ransom, S. M., Stairs, I. H., Backer, D. C., Greenhill, L. J., Bassa, C. G., Hessels, J. W. T., & Kaspi, V. M. 2004, *ApJ*, 604, 328
- Richer, H. B., Fahlman, G. G., & Vandenberg, D. A. 1988, *ApJ*, 329, 187
- Romani, R. W. 1987, *ApJ*, 313, 718
- Rutledge, R. E., Bildsten, L., Brown, E. F., Pavlov, G. G., & Zavlin, V. E. 1999, *ApJ*, 514, 945
- . 2002, *ApJ*, 578, 405
- Rybicki, G. B., Heinke, C. O., Narayan, R., & Grindlay, J. E. 2005, *ApJ*, submitted
- Sandquist, E. L., Bolte, M., Langer, G. E., Hesser, J. E., & Mendes de Oliveira, C. 1999, *ApJ*, 518, 262
- Sosin, C. 1997, *AJ*, 114, 1517
- Taylor, J. M., Grindlay, J. E., Edmonds, P. D., Cool, A. C., Cohn, H. N., & Lugger, P. M. 2005, *ApJ*, submitted
- Verbunt, F. 2001, *A&A*, 368, 137
- Verbunt, F., & Hut, P. 1987, in *IAU Symp. 125: The Origin and Evolution of Neutron Stars*, 187+—
- Yanny, B., Guhathakurta, P., Schneider, D. P., & Bahcall, J. N. 1994, *ApJ*, 435, L59
- Zavlin, V. E., Pavlov, G. G., & Shibanov, Y. A. 1996, *A&A*, 315, 141

TABLE 1
M30 X-RAY SOURCE PROPERTIES

Source	ID	Type, [redshift]	RA (h m s err)	Dec (° ' " err)	r (')	Cts (0.3–7 keV)	C_1	C_2	F_X (0.5–6 keV)	F_X (0.5–2.5 keV)	Name (positional part)
(1)	(2)	(3)	(4)	(5)	(6)	(7)	(8)	(9)	(10)	(11)	(12)
Sources within r_h; designated CXOGLB J...											
1	A2	CV?	21:40:22.186 0.003	−23:10:47.20 0.03	0.01	37.9 $^{+7.2}_{-6.1}$	0.23 $^{+0.41}_{-0.41}$	−0.11 $^{+0.57}_{-0.58}$	6.2 $^{+3.1}_{-1.4}$	3.8 $^{+1.3}_{-0.8}$	214022.18-231047.2
2	A1	qLMXB	21:40:22.130 0.001	−23:10:45.57 0.01	0.03	900.8 $^{+31.0}_{-30.0}$	−0.95 $^{+0.08}_{-0.08}$	−1.31 $^{+0.17}_{-0.17}$	65.5 $^{+2.7}_{-2.4}$	65.5 $^{+2.7}_{-2.4}$	214022.13-231045.5
3	A3		21:40:21.995 0.006	−23:10:47.21 0.09	0.03	9.9 $^{+4.3}_{-3.1}$	0.01 $^{+0.90}_{-0.90}$	−0.44 $^{+1.38}_{-1.48}$	1.0 $^{+0.6}_{-0.3}$	1.0 $^{+0.6}_{-0.3}$	214021.99-231047.2
4	B	CV	21:40:22.153 0.002	−23:10:51.66 0.04	0.07	97.6 $^{+10.9}_{-9.9}$	0.74 $^{+0.26}_{-0.26}$	−0.04 $^{+0.30}_{-0.30}$	12.7 $^{+2.9}_{-1.8}$	7.0 $^{+1.1}_{-0.8}$	214022.15-231051.6
5	C	CV	21:40:22.929 0.002	−23:10:49.25 0.03	0.19	122.5 $^{+12.1}_{-11.1}$	0.96 $^{+0.24}_{-0.24}$	0.87 $^{+0.28}_{-0.28}$	20.1 $^{+3.4}_{-2.4}$	7.9 $^{+1.2}_{-0.9}$	214022.92-231049.2
6			21:40:21.482 0.011	−23:10:54.57 0.06	0.19	7.6 $^{+3.9}_{-2.7}$	−0.54 $^{+1.06}_{-1.12}$	> −0.15	1.0 $^{+0.9}_{-0.4}$	0.5 $^{+0.6}_{-0.2}$	214021.48-231054.5
7		AB?	21:40:21.564 0.015	−23:10:32.60 0.12	0.28	4.6 $^{+3.3}_{-2.1}$	−0.44 $^{+1.41}_{-1.50}$	> 0.50	0.3 $^{+0.3}_{-0.1}$	0.3 $^{+0.3}_{-0.1}$	214021.56-231032.6
8			21:40:22.109 0.011	−23:11:14.10 0.10	0.45	11.7 $^{+4.5}_{-3.4}$	0.75 $^{+0.89}_{-0.84}$	1.19 $^{+1.33}_{-1.16}$	2.0 $^{+2.0}_{-0.7}$	0.9 $^{+0.5}_{-0.3}$	214022.10-231114.1
9			21:40:20.363 0.014	−23:10:22.88 0.13	0.57	6.6 $^{+3.7}_{-2.5}$	−0.97 $^{+1.21}_{-1.37}$	< 0.47	0.4 $^{+0.3}_{-0.2}$	0.4 $^{+0.3}_{-0.2}$	214020.36-231022.8
10		AB?	21:40:23.216 0.007	−23:09:58.49 0.12	0.85	6.5 $^{+3.7}_{-2.5}$	0.34 $^{+1.19}_{-1.15}$	−0.01 $^{+1.64}_{-1.64}$	0.6 $^{+0.7}_{-0.3}$	0.3 $^{+0.3}_{-0.1}$	214023.21-230958.4
11			21:40:19.361 0.012	−23:11:24.38 0.16	0.89	5.6 $^{+3.5}_{-2.3}$	> −1.08	0.74 $^{+1.41}_{-1.28}$	1.0 $^{+0.9}_{-0.4}$	0.4 $^{+0.6}_{-0.2}$	214019.36-231124.3
12			21:40:26.981 0.015	−23:10:38.84 0.16	1.13	5.6 $^{+3.5}_{-2.3}$	1.81 $^{+1.92}_{-1.63}$	1.51 $^{+1.96}_{-1.66}$	0.9 $^{+1.1}_{-0.4}$	0.3 $^{+0.3}_{-0.1}$	214026.98-231038.8
13			21:40:26.546 0.005	−23:11:18.26 0.05	1.14	14.6 $^{+4.9}_{-3.8}$	2.94 $^{+1.82}_{-1.47}$	2.81 $^{+1.83}_{-1.45}$	6.0 $^{+2.8}_{-1.8}$	0.2 $^{+0.3}_{-0.1}$	214026.54-231118.2
Sources outside of r_h; designated CXOU J...											
14			21:40:17.349 0.011	−23:11:34.13 0.08	1.35	6.5 $^{+3.7}_{-2.5}$	0.99 $^{+1.38}_{-1.22}$	0.43 $^{+1.50}_{-1.41}$	1.1 $^{+1.2}_{-0.4}$	0.5 $^{+0.6}_{-0.2}$	214017.34-231134.1
15			21:40:23.831 0.015	−23:09:20.30 0.15	1.50	5.5 $^{+3.5}_{-2.3}$	1.76 $^{+1.92}_{-1.64}$	> −0.79	1.6 $^{+2.0}_{-0.7}$	0.4 $^{+0.6}_{-0.2}$	214023.83-230920.3
16		QSO, 2.43	21:40:16.055 0.004	−23:09:57.36 0.03	1.63	98.4 $^{+11.0}_{-9.9}$	−0.20 $^{+0.24}_{-0.24}$	−0.56 $^{+0.38}_{-0.39}$	8.6 $^{+2.3}_{-1.1}$	6.9 $^{+1.1}_{-0.8}$	214016.05-230957.3
17	D	QSO?	21:40:29.235 0.001	−23:10:31.30 0.01	1.65	1850.7 $^{+44.0}_{-43.0}$	0.25 $^{+0.05}_{-0.05}$	0.22 $^{+0.07}_{-0.07}$	195.2 $^{+7.4}_{-6.6}$	111.2 $^{+3.4}_{-3.2}$	214029.23-231031.3
18			21:40:22.946 0.017	−23:09:06.09 0.10	1.70	4.3 $^{+3.2}_{-2.0}$	> −0.77	> −0.77	1.3 $^{+1.9}_{-0.6}$	0.3 $^{+0.6}_{-0.2}$	214022.94-230906.0
19			21:40:20.815 0.003	−23:12:29.93 0.07	1.74	33.7 $^{+6.9}_{-5.8}$	1.91 $^{+0.68}_{-0.63}$	1.04 $^{+0.55}_{-0.53}$	6.4 $^{+2.7}_{-1.5}$	2.6 $^{+0.9}_{-0.6}$	214020.81-231229.9
20			21:40:28.337 0.011	−23:09:29.96 0.17	1.92	13.5 $^{+4.8}_{-3.6}$	1.41 $^{+1.00}_{-0.90}$	1.61 $^{+1.28}_{-1.09}$	2.6 $^{+2.1}_{-1.0}$	1.0 $^{+0.7}_{-0.3}$	214028.33-230929.9
21			21:40:18.345 0.005	−23:12:32.20 0.07	1.95	32.6 $^{+6.8}_{-5.7}$	1.24 $^{+0.54}_{-0.52}$	0.43 $^{+0.54}_{-0.53}$	4.0 $^{+1.6}_{-0.8}$	2.4 $^{+0.8}_{-0.5}$	214018.34-231232.2

TABLE 1 — *Continued*

Source	ID	Type, [redshift]	RA (h m s err)	Dec ($^{\circ}$ ' " err)	r (')	Cts (0.3–7 keV)	C_1	C_2	F_X (0.5–6 keV)	F_X (0.5–2.5 keV)	Name (positional part)
(1)	(2)	(3)	(4)	(5)	(6)	(7)	(8)	(9)	(10)	(11)	(12)
22			21:40:29.878 0.008	−23:09:57.06 0.23	1.97	$7.3^{+3.8}_{-2.6}$	$1.27^{+1.41}_{-1.21}$	> -1.07	$2.3^{+2.0}_{-1.0}$	$0.2^{+0.3}_{-0.1}$	214029.87-230957.0
23			21:40:14.055 0.018	−23:11:42.50 0.10	2.07	$5.5^{+3.5}_{-2.3}$	$-0.78^{+1.29}_{-1.43}$	$0.00^{+2.42}_{-2.42}$	$0.6^{+0.7}_{-0.3}$	$0.3^{+0.3}_{-0.1}$	214014.05-231142.5
24			21:40:30.959 0.016	−23:10:18.78 0.13	2.08	$11.4^{+4.5}_{-3.3}$	> -1.93	> -1.93	$4.7^{+2.6}_{-1.5}$	$0.4^{+0.6}_{-0.3}$	214030.95-231018.7
25			21:40:18.087 0.012	−23:12:40.51 0.12	2.11	$6.6^{+3.7}_{-2.5}$	$1.05^{+1.41}_{-1.23}$	$-0.45^{+1.39}_{-1.49}$	$0.7^{+0.9}_{-0.3}$	$0.3^{+0.3}_{-0.1}$	214018.08-231240.5
26			21:40:15.717 0.003	−23:09:11.73 0.03	2.17	$200.8^{+15.2}_{-14.2}$	$0.69^{+0.17}_{-0.17}$	$0.50^{+0.21}_{-0.21}$	$23.3^{+3.1}_{-2.1}$	$14.5^{+1.5}_{-1.3}$	214015.71-230911.7
27		QSO, 3.08	21:40:15.015 0.004	−23:12:17.56 0.04	2.22	$83.5^{+10.2}_{-9.1}$	$0.52^{+0.27}_{-0.27}$	$-0.01^{+0.34}_{-0.34}$	$9.5^{+2.5}_{-1.4}$	$6.1^{+1.1}_{-0.8}$	214015.01-231217.5
28			21:40:32.027 0.009	−23:11:46.94 0.29	2.48	$5.6^{+3.5}_{-2.3}$	> -1.09	> -1.09	$1.3^{+1.0}_{-0.5}$	$0.8^{+0.7}_{-0.4}$	214032.02-231146.9
29			21:40:12.567 0.015	−23:09:36.80 0.12	2.49	$19.0^{+5.4}_{-4.3}$	$2.47^{+1.30}_{-1.06}$	$2.28^{+1.26}_{-1.04}$	$4.3^{+2.5}_{-1.2}$	$1.4^{+0.8}_{-0.4}$	214012.56-230936.8
30			21:40:33.237 0.006	−23:10:21.26 0.10	2.59	$44.2^{+7.7}_{-6.6}$	$2.06^{+0.61}_{-0.57}$	$0.87^{+0.45}_{-0.44}$	$7.6^{+2.0}_{-1.4}$	$2.8^{+0.9}_{-0.6}$	214033.23-231021.2
31			21:40:31.449 0.009	−23:09:15.06 0.09	2.63	$28.1^{+6.4}_{-5.3}$	$0.37^{+0.49}_{-0.49}$	$0.64^{+0.71}_{-0.68}$	$4.5^{+2.3}_{-1.1}$	$1.9^{+0.8}_{-0.4}$	214031.44-230915.0
32			21:40:20.941 0.009	−23:08:01.43 0.07	2.78	$91.6^{+10.6}_{-9.6}$	$0.16^{+0.25}_{-0.25}$	$0.42^{+0.36}_{-0.36}$	$10.7^{+2.6}_{-1.5}$	$6.4^{+1.1}_{-0.8}$	214020.94-230801.4
33			21:40:16.192 0.004	−23:08:19.79 0.03	2.81	$357.6^{+19.9}_{-18.9}$	$0.10^{+0.12}_{-0.12}$	$0.62^{+0.18}_{-0.18}$	$39.9^{+3.9}_{-2.9}$	$23.8^{+1.8}_{-1.6}$	214016.19-230819.7
34			21:40:21.699 0.008	−23:13:36.09 0.17	2.82	$11.8^{+4.5}_{-3.4}$	$1.19^{+1.01}_{-0.92}$	$1.36^{+1.31}_{-1.13}$	$4.7^{+4.4}_{-1.7}$	$1.2^{+0.8}_{-0.4}$	214021.69-231336.0
35			21:40:09.644 0.021	−23:10:46.20 0.17	2.87	$5.9^{+3.6}_{-2.4}$	> -1.23	> -1.23	$2.9^{+2.4}_{-1.1}$	$0.2^{+0.5}_{-0.2}$	214009.64-231046.2
36			21:40:34.509 0.012	−23:09:47.00 0.25	3.02	$9.1^{+4.1}_{-2.9}$	$2.52^{+1.74}_{-1.58}$	$2.28^{+1.87}_{-1.53}$	$2.2^{+1.9}_{-0.7}$	$1.0^{+0.8}_{-0.4}$	214034.50-230947.0
37			21:40:30.865 0.005	−23:13:08.23 0.10	3.09	$38.8^{+7.3}_{-6.2}$	$3.10^{+1.20}_{-0.98}$	$0.93^{+0.47}_{-0.45}$	$19.9^{+6.4}_{-3.9}$	$4.9^{+2.1}_{-1.1}$	214030.86-231308.2
38			21:40:32.697 0.014	−23:08:48.88 0.27	3.13	$9.9^{+4.3}_{-3.1}$	$0.23^{+0.91}_{-0.89}$	> -1.01	$2.0^{+2.0}_{-0.7}$	$0.8^{+0.7}_{-0.3}$	214032.69-230848.8
39		star ^a	21:40:33.308 0.004	−23:12:36.35 0.09	3.15	$56.5^{+8.6}_{-7.5}$	$-1.22^{+0.38}_{-0.39}$	$-1.01^{+0.81}_{-0.86}$	$5.2^{+1.1}_{-0.7}$	$5.2^{+1.1}_{-0.7}$	214033.30-231236.3
40			21:40:08.371 0.020	−23:11:18.99 0.13	3.20	$10.6^{+4.4}_{-3.2}$	$1.92^{+1.45}_{-1.19}$	$0.38^{+0.97}_{-0.94}$	$1.8^{+2.0}_{-0.7}$	$0.9^{+0.7}_{-0.3}$	214008.37-231118.9
41			21:40:08.077 0.028	−23:11:30.69 0.16	3.31	$9.2^{+4.2}_{-3.0}$	$1.65^{+1.37}_{-1.15}$	> -1.49	$2.4^{+2.0}_{-0.9}$	$0.4^{+0.4}_{-0.2}$	214008.07-231130.6
42			21:40:33.483 0.017	−23:08:31.67 0.16	3.45	$4.7^{+3.3}_{-2.1}$	$2.02^{+1.07}_{-1.78}$	$-1.60^{+1.71}_{-1.93}$	$0.7^{+0.9}_{-0.3}$	$0.4^{+0.3}_{-0.2}$	214033.48-230831.6
43			21:40:09.366 0.014	−23:08:50.84 0.22	3.52	$13.0^{+4.7}_{-3.6}$	$0.45^{+0.78}_{-0.76}$	$1.31^{+1.38}_{-1.18}$	$2.1^{+2.0}_{-0.9}$	$0.9^{+0.7}_{-0.3}$	214009.36-230850.8
44			21:40:24.403 0.009	−23:14:20.38 0.22	3.59	$11.6^{+4.5}_{-3.4}$	> -1.93	> -1.93	$4.8^{+2.5}_{-1.4}$	$0.4^{+0.7}_{-0.3}$	214024.40-231420.3
45			21:40:16.223 0.011	−23:07:18.45 0.08	3.73	$87.4^{+10.4}_{-9.3}$	$0.28^{+0.26}_{-0.26}$	$0.44^{+0.36}_{-0.36}$	$8.8^{+1.9}_{-1.2}$	$6.5^{+1.2}_{-0.9}$	214016.22-230718.4

TABLE 1 — *Continued*

Source	ID	Type, [redshift]	RA (h m s err)	Dec ($^{\circ}$ ' " err)	r (')	Cts (0.3–7 keV)	C_1	C_2	F_X (0.5–6 keV)	F_X (0.5–2.5 keV)	Name (positional part)
(1)	(2)	(3)	(4)	(5)	(6)	(7)	(8)	(9)	(10)	(11)	(12)
46			21:40:21.436 0.018	−23:06:50.14 0.15	3.95	43.1 $^{+7.6}_{-6.5}$	2.82 $^{+0.90}_{-0.78}$	1.92 $^{+0.61}_{-0.57}$	9.3 $^{+3.0}_{-1.8}$	3.3 $^{+1.1}_{-0.7}$	214021.43-230650.1
47			21:40:21.558 0.012	−23:14:49.49 0.15	4.04	16.5 $^{+5.1}_{-4.0}$	1.29 $^{+0.84}_{-0.78}$	0.86 $^{+0.87}_{-0.82}$	4.0 $^{+2.3}_{-1.1}$	1.4 $^{+0.9}_{-0.4}$	214021.55-231449.4
48			21:40:20.501 0.013	−23:15:05.59 0.25	4.32	14.4 $^{+4.9}_{-3.7}$	0.44 $^{+0.74}_{-0.72}$	0.22 $^{+0.98}_{-0.96}$	2.2 $^{+1.3}_{-0.6}$	1.8 $^{+0.9}_{-0.5}$	214020.50-231505.5
49			21:40:03.419 0.020	−23:11:34.42 0.15	4.37	28.1 $^{+6.4}_{-5.3}$	0.71 $^{+0.52}_{-0.51}$	−0.38 $^{+0.62}_{-0.63}$	9.2 $^{+4.1}_{-1.9}$	6.5 $^{+2.4}_{-1.4}$	214003.41-231134.4
50		Ellipt., 0.27	21:40:37.036 0.012	−23:13:37.17 0.31	4.44	13.1 $^{+4.7}_{-3.6}$	1.42 $^{+1.01}_{-0.91}$	0.59 $^{+0.93}_{-0.88}$	3.2 $^{+2.1}_{-0.9}$	0.9 $^{+0.6}_{-0.3}$	214037.03-231337.1

NOTE. — Properties of X-ray sources in M30. Energy bands for counts and fluxes are in keV. X-ray fluxes (corrected for photoelectric absorption of $1.7 \times 10^{20} \text{ cm}^{-2}$) are in units of $10^{-15} \text{ erg s}^{-1} \text{ cm}^{-2}$. See §§3.2,3.3 for details.

^a Bright foreground star.